

Effect of Chest Morphology on Vibrational Cardiography Waveforms using Multi-Sensor Analysis

Siddiqui Azizul Hakim

Department of Electrical & Computer Engineering

McGill University

Montreal, Canada

August 2021

A thesis submitted to McGill University in partial fulfillment of the requirements of the degree
of Master of Science

© 2021 Siddiqui Azizul Hakim

ABSTRACT

Vibrational waves generated by cardiac events can be detected by an accelerometer or a gyroscope placed on the surface of the chest. These waves are generally in the infrasonic range and contain information about cardiac mechanics. Recent advances in sensor technology have paved the way to portable, and non-invasive sensors. Wearable devices developed with these sensors can be used to monitor cardiac vibrations continuously, providing early detection of cardiovascular diseases. These are especially important in rural areas or even for astronauts in the space, that is, in places where proper clinical support is often unavailable. However, these vibrations are extremely sensitive to sensor placement. Hence a better understanding of the waves in connection the human body is necessary to take this system from the lab to a hospital setting, and our households. This thesis studies cardiac vibrations through acceleration recorded on seven locations on the chest. Previous studies have attempted to investigate chest vibrations through physical testing, analytical solution, and simulation. However, any connection between morphological changes in the chest and vibrational cardiography (VCG) signal quality is yet to be established. In this study, we propose a novel method to connect the vibrations to the changes in body composition level by testing in the lab, and by building simple numerical models of the human chest containing individual material properties for the organs within. A multi-sensor based simultaneous VCG recording system was developed in the lab and detailed in this thesis. A pilot test was performed on three subjects at McGill University, during the restrictions placed by the Covid-19 pandemic. One participant underwent a weight loss and strength training program and testing revealed that the signal-to-noise ratio of cardiac vibrations improved during that period. Amplitude modulation due to different sensor positioning was observed and it helped to identify the best locations on the chest for VCG recording. All sensor positions were able to pick up cardiac valvular activity. The systolic and the diastolic peak of the vibrational waves were studied simultaneously in time and frequency domain and revealed similar frequency contents in the signal during both events. A detailed study on a larger population must be completed to validate the findings.

RÉSUMÉ

Les ondes vibratoires générées par les événements cardiaques peuvent être détectées par un accéléromètre ou un gyroscope placé à la surface du thorax. Ces ondes sont généralement dans la gamme infrasonore et contiennent des informations sur la mécanique cardiaque. Les progrès récents de la technologie des capteurs ont ouvert la voie à des capteurs portables et non invasifs. Les dispositifs portables développés avec ces capteurs peuvent être utilisés pour surveiller les vibrations cardiaques en continu, permettant une détection précoce des maladies cardiovasculaires. Ceux-ci sont particulièrement importants dans les zones rurales ou même pour les astronautes dans l'espace, c'est-à-dire dans des endroits où un service de santé approprié n'est pas souvent disponible. Cependant, ces vibrations sont extrêmement sensibles au placement du capteur. Par conséquent, une meilleure compréhension de ces ondes en relation avec le corps humain est nécessaire pour faire passer ce système du laboratoire au milieu hospitalier, et dans nos maisons. Cette thèse étudie les vibrations cardiaques grâce aux accélérations enregistrées à sept endroits différents de la poitrine. Des études antérieures ont tenté d'étudier ces vibrations à travers d'un test physiques, d'une solution analytique et d'une simulation. Cependant, aucun lien entre les changements morphologiques de la poitrine et la qualité du signal de cardiographie vibratoire (VCG) n'a pas encore été établi. Dans cette étude, nous proposons une nouvelle méthode pour relier les vibrations aux changements de niveau de composition corporelle grâce à des résultats obtenus au laboratoire et grâce à des modèles numériques de la poitrine humaine contenant les propriétés des organes. Un système d'enregistrement VCG simultané basé sur plusieurs capteurs a été développé en laboratoire et détaillé dans cette thèse. Un test pilote a été réalisé sur trois sujets à l'Université McGill, pendant les restrictions imposées par la pandémie de Covid-19. Un participant a suivi un programme de perte de poids et de musculation et les tests ont révélé que le rapport entre le signal et le bruit des vibrations cardiaques s'est amélioré au cours de cette période. Une modulation d'amplitude due au positionnement différent du capteur a été observée et a permis d'identifier les meilleurs emplacements sur la poitrine pour les enregistrements VCG. Tous les placements des capteurs étaient capables d'enregistrer l'activité valvulaire cardiaque. Les apogées systolique et diastolique des ondes vibrationnelles ont été étudiés simultanément dans le domaine temporel et fréquentiel et nous avons découvert des contenus de fréquence similaires dans le signal

pendant les deux événements. Une étude détaillée sur une population plus large doit être réalisée pour valider les résultats.

ACKNOWLEDGMENTS

I would like to thank my supervisor Prof. Dr. David V. Plant for the opportunity to develop this thesis. His constant support and belief allowed me and my colleagues to set up a biomedical sensing team within his photonics systems group at McGill. Dave takes constant care of his students, and it was especially noticeable during the Covid-19 pandemic. Dave also provides his graduate students with ample opportunity to grow and find their own path in the world of research. He is an exemplary professor and a widely respected researcher.

It has been a great pleasure to also be supported by Michel Lortie and the MDA Corporations for the project. I am thankful to Michel for the guidance and supervision.

Yannick D'Mello and James Skoric have provided me with constant support, and their valuable friendship. We started our journey as colleagues, and ended up becoming more than brothers. This thesis would not be possible without their effort.

Ezz Aboulez has supported the sensor design and data acquisition coding. Nathan Clairmonte assisted with data collection. I am also very grateful to them for their friendship throughout the years. Santiago Bernal has also been part of the journey without being directly involved in the project.

I would like to thank my parents and my two amazing sisters for their constant support throughout my many years at McGill. As an international student thousands of miles away from home, it was always a constant challenge. In 2016 my mother fell sick and was bedridden for almost a year. While I wanted to drop out from university and return home, she gave me constant motivation to continue my studies. The struggle built a resilience in me that still keeps me going during difficult times. I am forever indebted to the best family anyone could have asked for. This thesis is dedicated to them.

I am grateful to Maria, Sanim, Tahsin, Asif, Shovan, Rafid, Saarah, Adhina, Shonamia, Adam, my fellow Bangladeshi students at McGill, my partners at our small start-up named Stocate, and all my other friends at home and abroad. I value each and everyone's friendship, guidance, and support.

AUTHOR CONTRIBUTIONS

This thesis was written by Siddiqui Azizul Hakim. All the chapters of this thesis represent work completed by myself. Yannick D'Mello, and James Skoric contributed to the project framework, the design of the studies, and the analysis methodology. James Skoric, Ezz Aboulez, Nathan Clairmonte contributed to data collection. Ezz Aboulez contributed to the sensor design and coding. French translation of the thesis abstract was completed by Santiago Bernal.

TABLE OF CONTENTS

Abstract	2
Résumé.....	3
Acknowledgments.....	5
Author Contributions	6
Table of Contents	7
List of Figures	10
List of Tables.....	12
List of Acronyms	13
I. Introduction	15
A. Motivation.....	15
B. Cardiac Function	16
1. Cardiac Beating	16
2. Cardiac Cycle	16
3. Cardiac Vibrations.....	17
C. Non-Invasive Cardiac Monitoring	17
1. Electrical.....	17
2. Optical	18
3. Mechanical.....	18
D. Thesis Objective.....	20
II. Data Acquisition Methods	22
A. Multi-Sensor Vibrational Cardiography.....	22
1. Sensor	22

2.	Connectivity.....	22
3.	Placement.....	23
B.	ECG.....	25
C.	Time-Correlated Data Collection	25
D.	Human Testing	26
E.	Pre-Processing.....	28
III.	Analysis.....	30
A.	Signal-to-Noise ratio (SNR).....	30
B.	Cardiac Timing.....	31
C.	Dominant Frequency	32
D.	Time-Frequency (TF) Analysis.....	33
1.	TF Representation.....	33
2.	TF Analysis.....	34
E.	Simulation of Cardiac Waveforms.....	35
1.	Geometry and Materials	36
2.	Physics	36
3.	Input Load.....	37
4.	Study and Mesh	37
IV.	Results.....	39
A.	Signal-to-Noise ratio	39
1.	SNR and Sensor Placement	39
2.	SNR During Weight Loss.....	40
B.	Cardiac Timing.....	41
C.	Dominant Frequency	42
D.	V1 and V2 Peak.....	43

1. Time.....	43
2. Frequency	44
E. Simulated VCG	45
V. Discussion.....	48
VI. Conclusion	51
VII. Appendix	52
A. SNR	52
B. IVCP, LVET, and IVRP.....	53
C. PCT.....	54
VIII. References	57

LIST OF FIGURES

Figure 1: Electrocardiography (Top) and dorso-ventral axis Vibrational Cardiography waveform (bottom) corresponding to one heart beat, with fiducial points marked.....	19
Figure 2: VCG measurement locations. From top: 1) AAr: Ascending aorta region. 2) AV: Aortic valve location. 3) PV: Pulmonary valve location. 4) Mid-Sternum: Approximately 4 cm between AAr and XP. 5) TV: Tricuspid valve location. 6) MV: Mitral valve location and situated at the apex of the heart. 7) XP: Xiphoid process region. Recreated from [58].....	24
Figure 3: A schematic (Recreated from [58]) of the system built to capture VCG data from seven different locations on the sternum with IMUs through a Raspberry Pi. ECG data was captured with the BIOPAC system (Electrode positions shown in blue circle). The data from both systems were simultaneously analyzed on a computer.....	25
Figure 4: (a) Dorso-ventral axis VCG plotted for all S-VCG locations (AAr, Mid-sternum, and XP), and the Heart apex. (b) RMS values of VCG signals corresponding to the same locations are plotted. The data was taken from an inhaled breath hold test. Both plots represent average data from 25 sequential heart beats.	30
Figure 5: Dorso-ventral axis VCG is plotted at the XP location. Key fiducial points identifiable in the waveform are marked. Data taken during an inhaled breath hold test from 25 sequential heart beats.	31
Figure 6: Frequency domain representation of a dorso-ventral axis VCG signal collected from a subject during the inhaled breath hold test. (a) VCG waveform in time represents average data from 25 sequential heart beats. (b) DFT (Top) and Pwelch (bottom) performed on the entire dataset. Both DFT and Pwelch method were able to identify the frequency peaks marked at 3, 11, and 26 Hz.	32
Figure 7: a) S-VCG locations. b) Average (25 heartbeats) dorso-ventral VCG collected from a subject in supine position during inhaled breath hold and corresponds to the locations shown in (a). c) Continuous wavelet transformation (Morse). d) Polynomial chirplet transformation. ..	34
Figure 8: a) PCT of dorso-ventral VCG collected in supine position during inhaled breath hold at XP location (Top). Time domain signal (bottom left) and 3D surface plot (bottom right) is shown. b) V1 and V2 peak in time. c) V1 and V2 peak in frequency.	35

Figure 9: (a) Input V1 and V2 pulse load. (b) Geometry with six different domains. Load was inputted in domain 1. (c) (Top) Surface plot of Acceleration propagation during the simulation. (Bottom) Acceleration value at Output node (skin layer) representing a synthetic VCG signal. 38

Figure 10: V1 SNR from three Sensor locations (TV, XP, and MV) for all the tests are plotted against the subject's BMI changes over 6 weeks. 41

Figure 11: The bar plot represents IVCP (in blue), LVET (in orange), and IVRP (grey) for all subjects at each location of the chest. The SD is plotted as vertical error bars. 42

Figure 12: (a) Simulated dorso-ventral axis VCG plotted for different fat layer thickness (domain 5). (b) RMS values corresponding to the different VCG waveform. 46

Figure 13: (a) Simulated dorso-ventral axis VCG plotted for different input domain elasticity. (b) RMS values corresponding to the different VCG waveform 47

LIST OF TABLES

Table 1: Participants of the multi-sensor VCG data collection	26
Table 2: Tests performed by each participant during data collection	27
Table 3: Wellness metrics gathered from subject 1 during the weight loss program	28
Table 4: Simulation geometry and material parameters	36
Table 5: Average SNR for all subjects during the different tests performed.....	39
Table 6: V1 and V2 SNR at XP, TV, and MV for Subject 1. Corrupted data due to system failure shown as empty cells	40
Table 7: Average dominant frequencies found for each subject.....	43
Table 8: Location of V1 and V2 peaks in time	43
Table 9: V1 and V2 peak widths in time.....	44
Table 10: Center frequency of V1 and V2	44
Table 11: Frequency widths of V1 and V2	45

LIST OF ACRONYMS

AAr	Ascending Aorta region
AV	Aortic Valve
BCG	Ballistocardiography
BMI	Basal Mass Index
BMR	Basal Metabolic Rate
CO	Cardiac Output
CT	Chirplet Transform
CTI	Cardiac timing interval
CVD	Cardiovascular diseases
CWT	Continuous Wavelet Transform
DFT	Discrete Fourier Transform
ECG	Electrocardiogram
FWHM	Full width half maximum
GCG	Gyrocardiography
ICG	Impedance Cardiography
IMU	Inertial Measurement Unit
IVCP	Isovolumetric contraction period
IVRP	Isovolumetric relaxation period
LVET	Left ventricular ejection time
MV	Mitral Valve
PCT	Polynomial Chirplet Transformation

PCG	Phonocardiography
PPG	Photoplethysmography
PV	Pulmonary Valve
Pwelch	Welch's power spectral density
RMS	Root mean squared
SCG	Seismocardiography
SD	Standard Deviation
SNR	Signal-to-noise ratio
SV	Stroke volume
S-VCG	Sternal VCG
TFD	Time-Frequency domain
TV	Tricuspid Valve
V1	VCG systolic peak
V2	VCG diastolic peak
V-VCG	Valvular VCG
VCG	Vibrational Cardiography
XP	Xiphoid process
WT	Wavelet transformation

I. INTRODUCTION

A. Motivation

Cardiovascular diseases (CVD) are a major cause of premature deaths [1] and are the second leading cause of deaths in Canada over the past 21 years [2]. CVD includes any disfunction of the heart and the surrounding blood vessels. Underlying CVD also increases the severity of respiratory diseases caused by viruses such as the beta-coronavirus [3]. Advances of modern technology in the medical field have reduced the possibility of a fatal outcome from CVD. While cases of CVD have increased 93% between 1990 and 2019, death rates caused by CVD have only increased by 54% during that time [4]. Continuous monitoring of heart functions can further reduce this mortality rate by providing improved early detection of critical physiological changes [5]. To develop such a system, a proper understanding of the body functions is necessary. But the inherent complexity and interconnected dependencies of the human body still raises many unanswered questions. While it might not be convenient to experiment on living human bodies to understand cardiac functions, relying on non-invasive examination have provided a lot of information-rich signals that can be analyzed to estimate the sources of irregularities. However, it is still cumbersome to perform non-invasive tests on human subjects, an issue intensified by the ongoing pandemic. In this regard, computationally modeling the human body and the heart can help explain key cardiac functions, leading to a better understanding of cardiac diseases and associated treatments [6].

The motivation behind the following thesis is divided into two parts. Firstly, it develops a system of wireless cardiac monitoring that can be easily replicated in different labs, and can be used to develop cost-effective solutions to provide cardiac assessment at home. The system captures data from multiple non-invasive sensors placed on the surface of the chest. Hence, it has been characterized based on sensor placement and signal quality. The effect of body composition on the captured signal was also explored. The second part of the thesis develops computationally efficient models that can emulate non-invasive analysis of the human body. The goal of developing the models is to verify the findings the in the lab.

A brief discussion about the functioning of the human heart and a detailed discussion about the current standards in cardiac monitoring are given below.

B. Cardiac Function

1. Cardiac Beating

The heart is one of the most vital organs in the human body. It pumps blood to oxygenate the body and to remove wastes via the circulatory system. A normal heart rate is approximately 60 to 90 beats per minute (1-1.5 Hz, or 1-1.5 beats per second) at rest, maximum 200 beats per minute during exercising, and around 500 beats per minute during atrial fibrillation [7]. The heart consists of four chambers (right and left atrium, and ventricle) that operates two pumps. Contraction and relaxation at the atrium and the ventricle of the heart is controlled by electrical impulses that are generated at the sinoatrial node [7]. The right ventricle, a low-pressure pump, supplies the pulmonary circulation, whereas the left ventricle, a high-pressure pump, supplies the systemic circulation. As the ventricles and the atriums contract and relax, the one-way valves connecting them opens and closes to allow blood flow. It is important to remember that these valves are passive, hydraulic devices. They do not contain any active muscle [8]. They move due to pressure differentials of blood. The whole process is controlled electrically and can be monitored using electrocardiography (ECG) [9]. The movement of the heart chambers are mechanical. During each beat, the heart performs a series of events that can be described as the cardiac cycle.

2. Cardiac Cycle

A cardiac cycle is divided into two major phases, ventricular contraction (systolic phase), and relaxation (diastolic phase). The heart pushes the blood into the body during systole, and refills during diastole [10]. At the beginning of the cardiac cycle, deoxygenated blood flows into the right atrium from the vena cava while oxygenated blood flows into the left atrium from the pulmonary veins. Blood flows from the right atrium to the right ventricle through the tricuspid valve and from left atrium to the left ventricular through the mitral valve. Both valves close because of reversed pressure differential when the ventricles are filled. The snap produces vibrational pulses, and can be heard as the first heart sound (S1). At this point, the ventricles contract while the pulmonary

and the aortic valves are still closed, increasing the pressure rapidly, resulting in isovolumetric contraction (IVCP). As pressure in the ventricles increase further, the pressure differentials cause the pulmonic and the aortic valve to open. This causes a rapid pulsatile ejection of blood through the aorta and the pulmonary artery. As ventricular pressure drops below the pressure in the pulmonary artery and the aorta, both valves close and produce the second heart sound (S2) [11]. The ventricles then start to relax with all valves closed, and ventricular pressure is decreased. This period is known as isovolumetric relaxation (IVRP). As ventricular pressure decreases below the atrium, the cycle is completed.

3. Cardiac Vibrations

While the heart sounds can be picked up from the surface of the chest with a stethoscope, the deformation of the heart during every heartbeat also generates infrasonic mechanical waves. The waves are assumed to be generated as a result of ventricular contraction, valvular activity, and pulsatile flow [12]. These waves diffuse through the organs and propagate to the surface of the body, and can be picked up by non-invasive monitoring as displacement, velocity, or acceleration [13, 14]. These signals have shown to provide important information on cardiovascular functions [15], and diseases [16]. A brief description on the current standards of non-invasive cardiac monitoring is given below, including a more detailed discussion on cardiac vibration analysis.

C. Non-Invasive Cardiac Monitoring

Several techniques have been proposed to monitor the heart non-invasively. The prominent ones are described here according to the underlying physics.

1. Electrical

ECG is the current clinical standard of cardiac monitoring. It is a measure of potential difference between electrodes that are placed on different parts of the chest. ECG was first introduced in 1901, and medical usage began around 1950 [17]. A sample ECG signal is provided by a graph of voltage (millivolts) vs. time (duration of a cardiac cycle) and is shown in Figure 1.

Electrical impulses generated at the sinoatrial node control contraction and relaxation at the atrium and the ventricle of the heart. The P, and the R peak represents the depolarization of the atrium, and the ventricle respectively. The T peak shows the repolarization of the ventricles [9]. Due to its ability to monitor heart rate [18], ECG can be used to detect arrhythmia [19], and ischemia [20]. While ECG is a valuable tool, it cannot be used to extract important cardiac information such as stroke volume (SV) and cardiac output (CO), which relate to the volume of blood ejected by the ventricle during a cardiac cycle. ECG has been measured from human subjects as a part of this thesis.

Measured similarly to ECG, Impedance Cardiography (ICG) is obtained by placing four electrode pairs around the neck and the thorax to record changes in the impedance. The outer (on the sagittal plane of the human body) electrodes are used to apply an alternating current, and the inner electrodes are used to measure the voltage differences across it [21]. ICG can monitor the flow of blood through the heart and provide information on SV and CO [22]. ECG and ICG are affected by motion artifact [23, 24].

2. Optical

Non-medical wearable fitness trackers such as Fitbit and Apple Watch uses Photoplethysmography (PPG) sensors placed on the hand to measure blood flow variation in the microvascular bed of tissue using a light-emitting diode and a photodetector [25]. It can detect heart rate [26], oxygen saturation [27], and arterial stiffness [28]. PPG is affected by motion artifact [29] and by ambient light [30].

3. Mechanical

The vibrations generated during the cardiac beating process can be detected as sounds via stethoscope auscultation or phonocardiography (PCG) [31]. This is often described as the ‘lub-dub’ that can be heard by placing one’s ear on another person’s chest. PCG can be correlated to ECG with very high accuracy [32], and typically is more rich in information than PPG [33].

The lower frequency mechanical (typically <50 Hz) vibrations can be detected by Seismocardiography (SCG), Gyrocardiography (GCG), and Ballistocardiography (BCG). BCG measures the ballistic forces of the heart in response to the blood flow during the cardiac beating

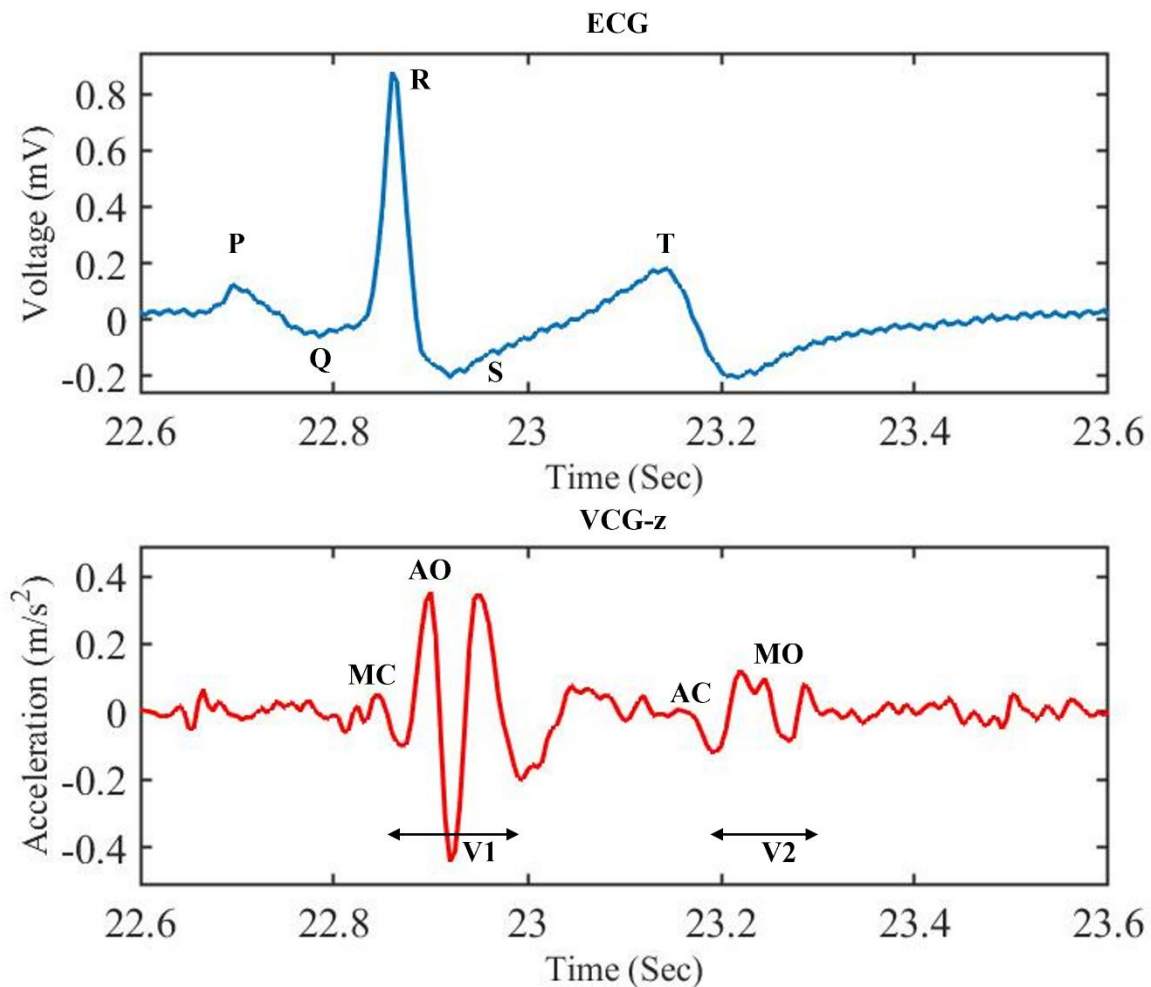


Figure 1: Electrocardiography (Top) and dorso-ventral axis Vibrational Cardiography waveform (bottom) corresponding to one heart beat, with fiducial points marked.

process. BCG is highly affected by subject's posture and can be challenging for post-processing [34]. While BCG measures the recoil forces of the body, SCG and GCG measures the local vibrations of the heart from the chest walls with an accelerometer, and a gyroscope respectively [35]. SCG was first introduced in 1964 [36] and further development started around 1990 [37]. A combination of tri-axis SCG and GCG is referred to as vibrational cardiography (VCG). The term was coined within the research group. VCG signal has been captured from human subjects in the lab as the focus of this thesis. VCG can provide unique insights into how cardiac muscles, and other tissues and organs behave in the propagation path of the infrasonic vibration. Cardiac timing intervals (CTIs) such as aortic and mitral valve opening and closing have been accurately predicted

by VCG [38]. VCG has been proposed to be a viable method of unobtrusive [39] cardiac monitoring [12, 35, 40].

Figure 1 provides a typical VCG waveform found in the dorso-ventral axis from a subject in a supine position. The waveform can be divided into two main events [16], V1 and V2, corresponding to the onset of the cardiac systole, and the diastole respectively. Key fiducial points such as mitral valve closing (MC), aortic valve opening (AO), aortic valve closing (AC), and mitral valve opening (MO) have been marked on the waveform based on previous work [41]. These points predict several key cardiac time intervals such as left ventricular ejection time (LVET) [42], IVCP, and IVRP [43]. LVET marks the time difference between AO and AC points in Figure 1 and represents the time required to eject blood from the ventricle to the aorta. IVCP represents the time difference between MC and AO, and IVRP represents the interval between AC and MO. However, these fiducial points are debated [44, 45], and no concrete proof has been found yet to connect these points to the assumed origins of the vibration. VCG has also been shown to be able to monitor respiration [46, 47]. However, it also means that VCG signals can be highly modulated by respiratory events and can be cumbersome to analyze. While VCG signals are known to be versatile cardiac monitoring tool, the acquired waveforms are highly affected by motion artifact [48], and sensor placement [49, 50]. Effect of body composition changes on the acquired signal still needs to be explored.

D. Thesis Objective

Several cardiac monitoring methods were discussed in the previous section. Among all the techniques, ECG and VCG data were captured in the lab from several participants. Several unanswered questions need to be tackled before VCG can be considered as a clinically viable method of cardiac monitoring. VCG signals are highly affected by sensor positioning, and depending on the needs of the system, different sensor locations can prove to be more useful to gather certain cardiac events [51]. This thesis studies different VCG capturing locations in the process of developing an easily deployable system for clinical and at home cardiac monitoring. Dorso-ventral axis VCG was analyzed for seven different locations of the chest. The gathered data was first compared based on their relative signal amplitude and it provided a measure for signal-

to-noise (SNR) ratio. SNR showed general improvement as one subject was measured multiple times over six weeks. During this period, the subject underwent a weight loss program. The collected data was used to correlate vibrations to subject's body mass index (BMI). Key cardiac event times were calculated from the recorded signal and compared between different locations. The signals were also studied in frequency domain where dominant frequencies corresponding to each waveform were extracted. Polynomial Chirplet Transform (PCT) and Continuous Wavelet Transform (CWT) were implemented to study the signal in both time and frequency domain simultaneously. PCT based time-frequency representation showed better amplitude concentration of the V1 and V2 peaks than CWT, and was further analyzed to the time and frequency widths of V1 and V2 at each location. Lastly, simple numerical based simulations were built to replicate and validate findings in the lab.

The development of the system is detailed in Chapter II. All analysis steps, and the simulation methodology are detailed in chapter III. The results are provided in chapter IV, and discussed in chapter V. Lastly, the thesis is concluded in chapter VI.

II. DATA ACQUISITION METHODS

This chapter explains the methodology and the techniques used to acquire information on cardiac activity from human test subjects. Both hardware and software aspects of the system have been explained in detail.

A. Multi-Sensor Vibrational Cardiography

1. *Sensor*

The system was designed to have the capabilities of being widely deployed for remote cardiac health monitoring. Hence, it was built with commercially available and cheap components that can be assembled with little complexity. The MPU-9250 by Invensense was used as the inertial measurement unit (IMU). The MPU-9250 has a small form factor and contains both a tri-axial accelerometer and a gyroscope that can be used simultaneously for six axes vibrational cardiography analysis. However, only the dorso-ventral axis accelerometer data was considered for analysis in this study, similar to previous works in the field [12, 35]. A total of four IMUs were used simultaneously to capture VCG data from different locations in the chest. The chosen IMU also has a high sampling rate (maximum 4000 Hz) and low RMS noise (0.078 m/s^2), making it ideal for capturing data in a wide range of scenarios [52]. The range of the accelerometer was set at $\pm 2 \text{ g}$ and the range of the gyroscope was set at $\pm 250 \text{ deg/sec}$.

2. *Connectivity*

To receive the data from the IMU, a Raspberry Pi (Pi-Zero W, Raspberry Pi) was used. Two IMUs were connected to one Pi and hence, two Pis were used to simultaneously run four IMUs. I2C data was polled by the Pi from each of the IMUs at an approximate rate of 300 Hz using a custom developed code. The Pi was chosen for its ability to process data from multiple IMUs together, and for being able to store the data on a memory card and wirelessly transmit that data to the computer device. The data received from each of the IMUs were appended in a single text file and was stored on a memory card on the Pi. This data was then sent to the computer device via Wi-Fi.

3. Placement

VCG signals can be picked up from different locations of the chest. However, the signal quality and the captured fiducial points vary based on the sensor's position on the chest [50, 53]. Testing multiple positions allowed us to verify and compare the effect of chest morphology on VCG with previous work in the field [49, 54, 55]. It also enabled the opportunity to find the best position for VCG measurement in a remote healthcare setting, where ease-of-use and unobtrusive setup is essential [56]. Seven locations on the chest surface were identified for data collection. The positions included three locations at the sternum, and the auscultation areas of the four heart valves [57]. These positions are marked in Figure 2 (recreated from [58]). Due to the limitation of maximum four sensors per simultaneous data collection, these positions were divided into two sets. Set one contained locations of interest on the sternum and was denoted as Sternal VCG (S-VCG). Set two contained valvular auscultation locations and was identified as valvular VCG (V-VCG).

The three S-VCG locations are marked as Xiphoid Process (XP), Mid-Sternum, and the Ascending Aorta region (AAr) in Figure 2. The XP location was chosen to be directly above the xiphoid process. It represents the cartilaginous section at the bottom of the sternum, detached from the ribs. The XP was picked as it was shown to be a reliable location for recording VCG signals [12], and as both V1 and V2 vibrations could be recorded at this location with good signal amplitude. Measuring this location also allowed our current data to be compared with our previous single sensor based VCG publications [14, 46, 59].

The AAr is located on the angle of Louis of the sternum. It is positioned at the level of the second costal ribs, between the T4 and the T5 thoracic vertebra [60]. The blood volume that is ejected from the left ventricle through the AV, flows through the ascending aorta into the other arteries of the body [10]. The elastic aorta vibrates because of this process and has the potential to be a possible source of the VCG signal. Hence, the AAr location was picked as it was the closest position on the sternum from the ascending aorta. To further verify the signal differences between XP and AAr, a midpoint approximately 4 cm between each sensor was selected and denoted as Mid-sternum. This location on the sternum was tested because of its close proximity to the AV, another possible source of VCG.

V-VCG locations are marked as the AV, PV, TV, and the MV/Heart Apex locations on Figure 2 and are positioned in the intercostal spaces of the ribs where each of the four heart valves are generally auscultated [57]. Vibrations due to each heart valve opening and closing can be heard and differentiated with a stethoscope at these locations. It was hypothesized that lower frequency vibrations were also best captured here.

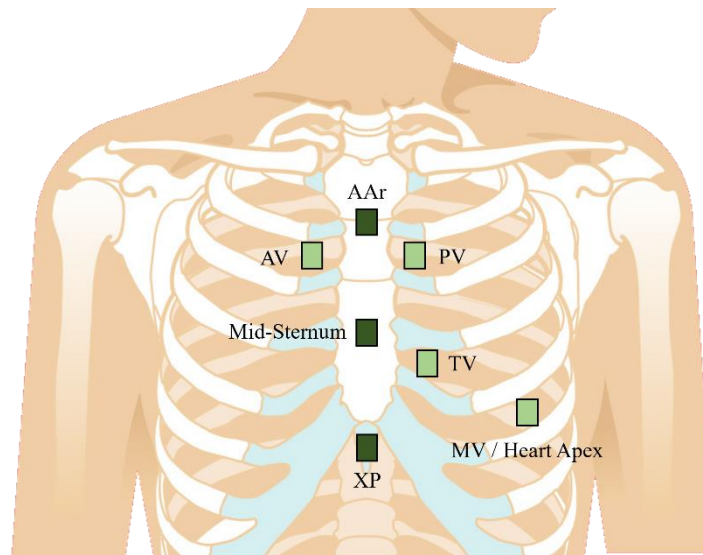


Figure 2: VCG measurement locations. From top: 1) AAr: Ascending aorta region. 2) AV: Aortic valve location. 3) PV: Pulmonary valve location. 4) Mid-Sternum: Approximately 4 cm between AAr and XP. 5) TV: Tricuspid valve location. 6) MV: Mitral valve location and situated at the apex of the heart. 7) XP: Xiphoid process region. Recreated from [58].

The second intercostal space on the right sternal border was used in previous studies as the aortic valve (AV) listening area [57], and was also selected for VCG acquisition because vibrations originating at aortic valve are transmitted here through minimum material discontinuities in the propagation path. The second intercostal space on the left sternal border was used as the pulmonary valve (PV) location. This location was selected because vibrations that can lead to the V2 event in VCG were found to be more pronounced on the left side of the heart [61]. The tricuspid valve (TV) VCG acquisition position was located on the fourth intercostal space on the right sternal border. TV location was picked as it was the closest to XP, but situated on the softer pectoral muscle instead of the cartilaginous xiphoid process.

The complex motion of the left ventricle was believed to be a possible source of modulation of VCG waveform through cardiac muscle contraction and blood flow turbulence. This was

investigated by placing a sensor at the fifth intercostal space medial to the clavicular line. It was denoted as the MV/Heart Apex location.

B. ECG

ECG (BN-RSPEC, BIOPAC) data was captured with the BIOPAC (BIOPAC, MP-160), a gold standard physiological measurement data acquisition device. ECG electrodes were placed at the corners of the Einthoven's triangular formation around the heart [62]. The AcqKnowledge software (AcqKnowledge 5, BIOPAC) was used to filter and smooth raw ECG data. The data acquisition methodology is shown in Figure 3.

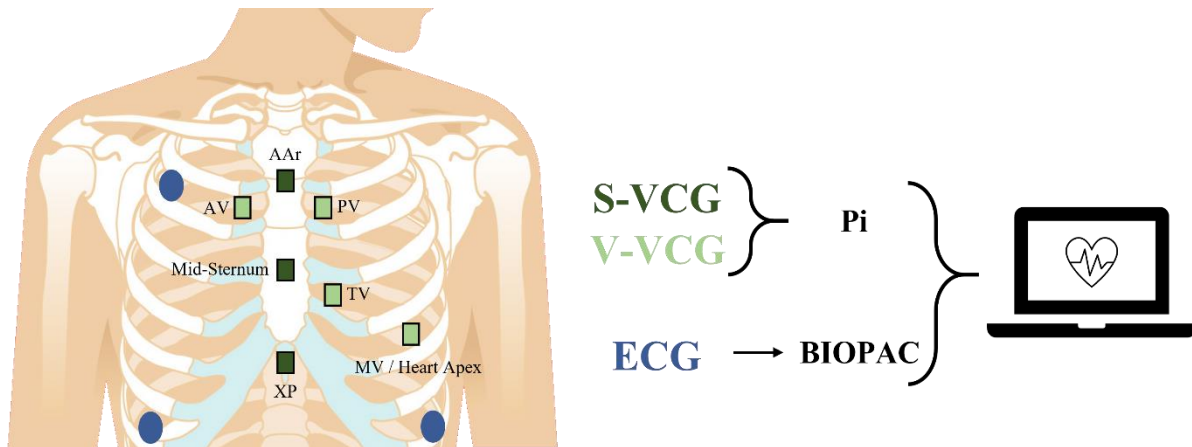


Figure 3: A schematic (Recreated from [58]) of the system built to capture VCG data from seven different locations on the sternum with IMUs through a Raspberry Pi. ECG data was captured with the BIOPAC system (Electrode positions shown in blue circle). The data from both systems were simultaneously analyzed on a computer.

C. Time-Related Data Collection

Time-correlation between each of the Pi, and the BIOPAC system was achieved with a clock signal generated by the BIOPAC. The clock consisted of a cycle of square waves of different pulse widths. The clock information was added as an additional channel of data and was collected simultaneously with ECG. This clock signal was also transmitted to both Pis through a physical wire. This technique created a reference timing between the BIOPAC and the Raspberry Pis. The

data from the Pis were appended to a text file and wirelessly accessed over Wi-Fi on a Windows 10 computer. The raw data file collected from each of the systems contained the global reference time information as a column. Matching both timeseries in MATLAB R2019a (MATLAB) provided the synchronization needed between each sensor, and the BIOPAC.

D. Human Testing

The multi-sensor VCG data was collected from three male participants. Due to safety concerns and restrictions placed on experiments involving human participants a result of the Covid-19 pandemic, a larger population data collection was not feasible. The participants were selected from the McGill student community. None of them had any prior cardiovascular diseases. The human trials were conducted with the approval of the research ethics board and department of electrical and computer engineering at McGill University. A future study has already been designed for a broader analysis with a larger set of participants. Table 1 provides basic information on the participants considered for data collection. Although data was collected only from three participants, Subject 1 was tested three times over six weeks. During this time, Subject 1 underwent a weight loss program and lost a total of 11.2 kg. The subject also performed 180 minutes of strength building exercises per week with a certified trainer. Strict sanitization and distancing (where possible) protocols were followed to reduce the potential of spreading the coronavirus during data collection in the lab. Each participant signed a consent form and reported their health status prior to entering the lab.

Table 1: Participants of the multi-sensor VCG data collection

Participant	Sex	Age (Years)	Weight (kg)	Height (m)
1	M	26	112.1 – 100.9	1.77
2	M	25	77	1.80
3	M	24	75.8	1.83

At the beginning of each test, the participants were briefed on the entire testing procedure. They were also given time to rest before the test started to reduce the possibility of an elevated heart rate during the test period. Three ECG electrodes were then placed on the torso as shown in Figure 3. The positive lead was attached to the electrode near the upper right of the torso. The negative lead was attached to the electrode placed near the bottom left of the torso. The ground

was attached to the final electrode near the bottom right of the torso. The IMUs were then placed in the appropriate position (either S-VCG or V-VCG) with double-sided tape. The X, Y, and Z axes of the sensors were oriented with the sinistro-dexter, inferior-superior, and dorso-ventral axes of the body respectively. In the S-VCG placement, the sensors were placed on the AAr, Mid-sternum, XP, and the MV/Heart apex locations as shown Figure 2 and 3. In the V-VCG orientation, the first three positions were changed to the AV, PV, and TV locations respectively. The MV/Heart apex position was identified by auscultation process with a stethoscope (Classic 3, 3M Littmann). Several positions were heard to interpret maximum amplitude of heart sound. The best location was picked based on the loudness of the heartbeat. As this required more time to set up than other locations where the data collection points were easily identifiable, the IMU placed on the MV/Heart apex location was kept unchanged throughout all six tests. All the tests were conducted with the participants being in a supine position to reduce motion artifact and noise while collecting data. During test 1 and test 4, participants were requested to breathe normally in a relaxed state. During test 2 and test 5, the participants were asked to inhale as much as possible and hold their breath for a maximum of 1 minute. During test 3 and test 6, the participants were asked to exhale as much as possible and hold their breath for a maximum of 1 minute. Table 2 lists the tests that each participant performed.

Table 2: Tests performed by each participant during data collection

Test	VCG sensor orientation	Test type	Maximum duration*	Breathing
1	S-VCG	Rest	1 Minute	Regular
2		High Lung Volume (HLV)	1 Minute	Inhaled hold
3		Low Lung Volume (LLV)	1 Minute	Exhaled Hold
4	V-VCG	Rest	1 Minute	Regular
5		High Lung Volume (HLV)	1 Minute	Inhaled hold
6		Low Lung Volume (LLV)	1 Minute	Exhaled Hold

* Participants may have stopped before

Over the six weeks of the weight loss program, the body composition of the Subject 1 was measured with a 3D body scanning machine (Body Scanner, FIT3D). During each measurement the scanner took 360-degree images of the subject to create a digital 3D image. FIT3D's proprietary algorithm then automatically measured the body area and fat composition levels, and transmitted the data to the subject over the cloud. Table 3 contains the physiological metrics of

subject 1 gathered during the weight loss program. VCG data was collected within one day of each 3D scan.

Table 3: Wellness metrics gathered from subject 1 during the weight loss program

Test	Waist Circumference	Chest Circumference	Body fat percentage	Weight	Fat Mass	Lean Mass	BMI	BMR
Week 1	120.4 cm	122.9 cm	42.03%	112.1 kg	47.1 kg	65 kg	35.8	2102
Week 3	116.6 cm	118.9 cm	38.56%	104.8 kg	40.4 kg	64.4 kg	33.4	2029
Week 6	113.3 cm	114.6 cm	37.1%	100.9 kg	37.5 kg	63.4 kg	32.2	1990
Reduction	7.1 cm	8.3 cm	4.93%	11.2 kg	9.6 kg	1.6 kg	3.6	112

Over the 6 weeks, the subject's body fat percentage decreased by almost 5%, fat mass reduced by 9.6 kg, and body mass index (BMI) improved by 10%. Body area also showed improvement, while lean mass and basal metabolic rate (BMR) showed deterioration. BMR represents the number of calories needed for basic functioning (breathing, blood circulation, body temperature, nervous function, muscle, and cell activity) of the body at rest [63].

E. Pre-Processing

Time correlated VCG and ECG were collected from all three participants and pre-processed in MATLAB before analysis. 30 minutes of cardiac data was collected for analysis. The captured data was first imported to MATLAB, even sampled at 500 Hz, and appended to a new time-series. The VCG data was then digitally filtered using a 3rd order Butterworth band-pass filter between 0.5 Hz and 55 Hz as VCG signals do not contain any cardiac information at high frequencies [16]. The lower frequency limit was set to remove respiration modulation, and any low frequency noise that would cause drifting in the signal. The higher frequency limit was set to remove noises from biological sources such as respiration and digestion sound, and also from systemic sources such as sensor noise and electrical connections. Data captured from the BIOPAC was filtered and smoothed with the AcqKnowledge 5 software before analysis. Due to inherent delays caused from manually turning on and off each of the Pis and the BIOPAC at the beginning and end of data collection, each data stream was carefully trimmed at the beginning and the end.

The different pulse widths in reference the clock was used to identify the starting and the ending points of the clock cycles reported by each system. Only the portion of the data that overlapped between all three sets (VCG from both Pis, and BIOPAC) were kept. Filtered and matched VCG, and BIOPAC data were further down sampled to 200 Hz for faster post-processing. VCG data was then separated and segmented by heartbeat. The ECG R peak was used to segment VCG signals according to each heartbeat. The Pan Tomkins real-time QRS analysis algorithm [64] was used for R peak detection. Each separated VCG waveform was selected to start 0.1s before the R peak to approximate the start of the cardiac cycle.

III. ANALYSIS

After filtering, down sampling, and segmentation, the following analysis were performed on the data collected from all seven locations. The analysis included both time and frequency domain feature extraction based on different positions and different tests performed.

A. Signal-to-Noise ratio (SNR)

SNR measures the relative quality of the acquired signal in comparison to the background noise. A low SNR signal is muffled with unwanted noise and can lead to inaccurate identification of V1 and V2. To get a metric for the signal quality, the amplitude of V1 and V2 portion of the VCG waveform was measured in relation to the noise. To acquire a measure of the noise from the signal, the portion of the VCG signal relating to the T-P interval of the ECG signal (Figure 1) was picked [49, 65]. This portion corresponds to a period when heart activity is low. During this period, the heart remains in a relaxed phase within the cardiac cycle and the VCG waveform shows very low acceleration variations over this period. Each segmented VCG signal was divided into three

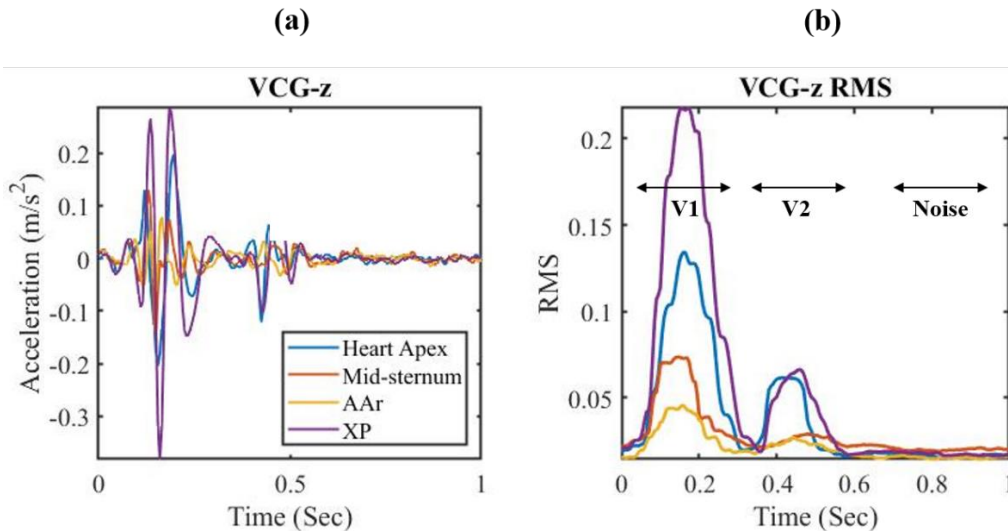


Figure 4: (a) Dorso-ventral axis VCG plotted for all S-VCG locations (AAr, Mid-sternum, and XP), and the Heart apex. (b) RMS values of VCG signals corresponding to the same locations are plotted. The data was taken from an inhaled breath hold test. Both plots represent average data from 25 sequential heart beats.

portions corresponding to V1 (Systolic period), V2 (Beginning of diastolic period), and noise (Cardiac dormancy/noise period), as shown in Figure 4.

The root mean squared (RMS) value of each of the segmented section was acquired using MATLAB's envelope function [66]. A sliding window of 100 ms was used and maximum RMS value acquired at each portion of the signal was extracted using MATLAB's findpeaks function. The SNR was measured using the following equation:

$$\begin{aligned} \text{VCG V1}_{\text{SNR}} &= \frac{\max(\text{rms VCG V1 period})}{\max(\text{rms Noise period})} \\ \text{VCG V2}_{\text{SNR}} &= \frac{\max(\text{rms VCG V2 period})}{\max(\text{rms Noise period})} \end{aligned} \quad (1)$$

B. Cardiac Timing

Cardiac timing intervals (CTIs) are clinically relevant information that provide insights on how the heart performs. Variability in CTIs can give important information on valve, artery, and myocardial diseases. Previous studies have shown VCG to be able to provide information on CTIs

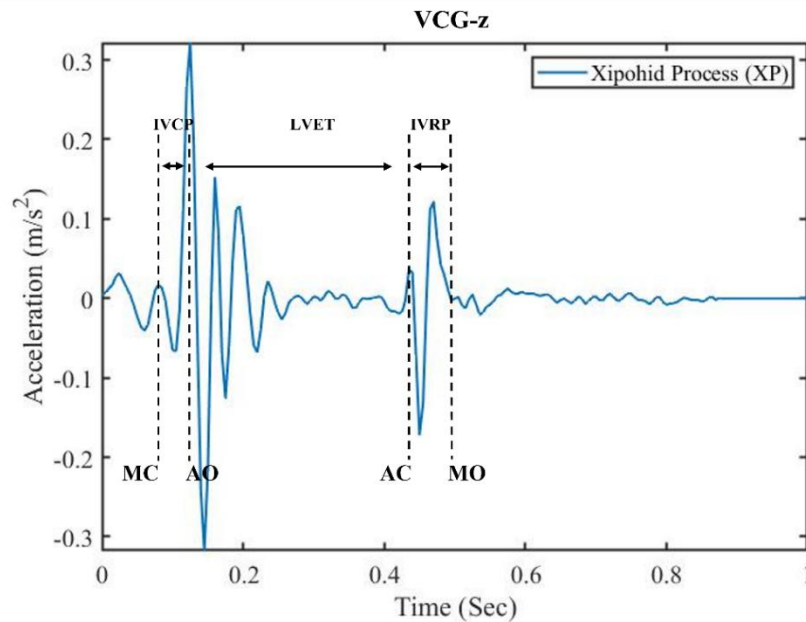


Figure 5: Dorso-ventral axis VCG is plotted at the XP location. Key fiducial points identifiable in the waveform are marked. Data taken during an inhaled breath hold test from 25 sequential heart beats.

[15, 44, 67]. The average VCG waveform in time domain was extracted for multiple subjects and MC, AO, AC, and MO fiducial points were marked [41] for all the locations on the chest for each of the tests. The data was then used to calculate LVET, IVCP, and IVRP as shown in Figure 5.

C. Dominant Frequency

To analyze the frequency content of VCG signals found in different chest locations, the dominant frequencies corresponding to each of the waves were extracted. For this, discrete Fourier transform (DFT) was computed using the MATLAB `fft` function. Due to the noisy recreation of the signal in frequency domain, Welch's power spectral density (Pwelch) estimate method (MATLAB `pwelch` function) was used to extract the power spectral density of the signal. A hamming window size of 750 ms was used. Both techniques were used to find the frequencies at each sensor location as shown in Figure 6.

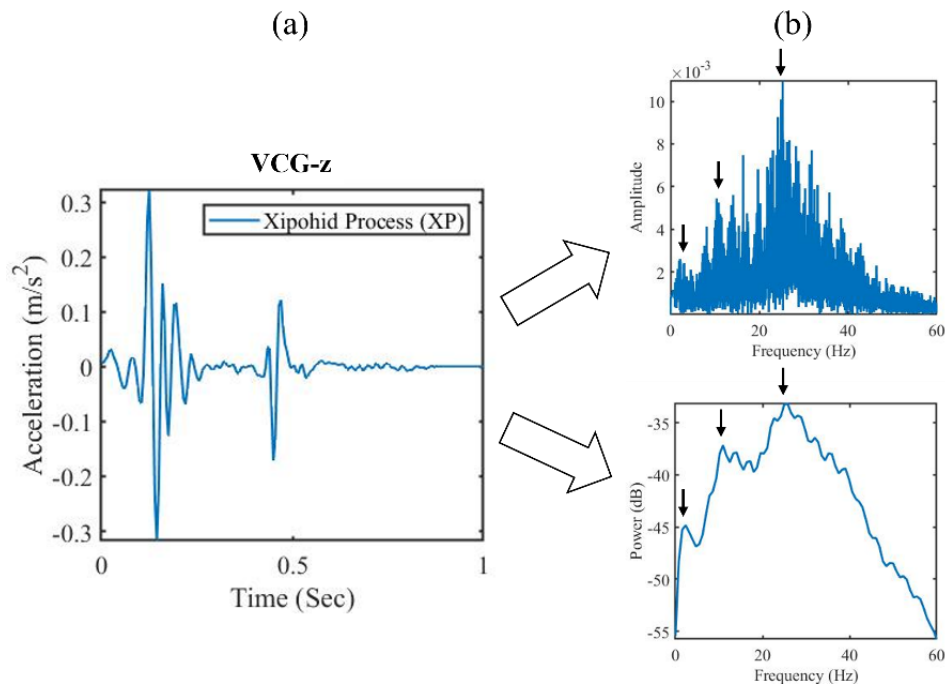


Figure 6: Frequency domain representation of a dorso-ventral axis VCG signal collected from a subject during the inhaled breath hold test. (a) VCG waveform in time represents average data from 25 sequential heart beats. (b) DFT (Top) and Pwelch (bottom) performed on the entire dataset. Both DFT and Pwelch method were able to identify the frequency peaks marked at 3, 11, and 26 Hz.

D. Time-Frequency (TF) Analysis

1. TF Representation

VCG signals records the physical process of heart movement, which is variable over time. Moreover, the signal is often dominated by noise. As a result, VCG signals contain periodic changes in both time and frequency domain. Recreating the signal only one domain is not adequate, and they should be studied together to retain the full contents of the signal. To create a time and frequency visualization of VCG signals, several spectral analysis methods have been proposed in previous works, such as short-time Fourier Transform [68], Continuous Wavelet Transform (CWT) [16], and Polynomial Chirplet Transform (PCT) [16, 49]. CWT is widely accepted as a time-frequency domain (TFD) analysis tool for studying many different biomedical signals such as ECG [69], PCG [70, 71], Electromyography (EMG) [72], Electroencephalogram (EEG) [73], and so on. CWT decomposes signals by small oscillations or wavelets (such as, Morse [73], Analytical morlet [74], or Bump [75]) that are localized in time and frequency domain. However, CWTs are affected by the Heisenberg–Gabor inequality [76], where improving the resolution of one of either time or frequency domains worsens the resolution in the other domain. PCT on the other hand was first introduced in 2011 [77] and builds on the conventional chirplet transform (CT) method [78] to analyze signals with non-linear instantaneous frequencies. An example of such a signal is the VCG waveform. Similar to CWT, chirplet transform also decomposes signals, but into small chirps instead of a wave. PCT incorporates nonlinear frequency rotating and shift operators, and a polynomial kernel to enhance the performance and resolution of TFD produced by CT [77]. The frequency rotating and shifting depends on the chirp rate parameter and it must be properly selected to match the chirp rate of the signal being analyzed. PCT based analysis have shown poor performance for multi-frequency component signals [77].

For developing the TFD of VCG signals, both CWT (Morse) and PCT was applied to the average VCG waveforms representing several heartbeats from each location. MATLAB's cwt function was used for wavelet transformation, and a modified version of a PCT function from [79] was used to perform PCT analysis. For PCT, the window length was set to 250 ms, frequency units were set to 10,000, and a chirp rate of 5 Hz/s was used. Both representations have been shown in

Figure 7 for S-VCG data captured from a subject during an inhaled breath hold test. While both representations showed comparable reconstruction of the VCG signal in TFD, CWT based TFD

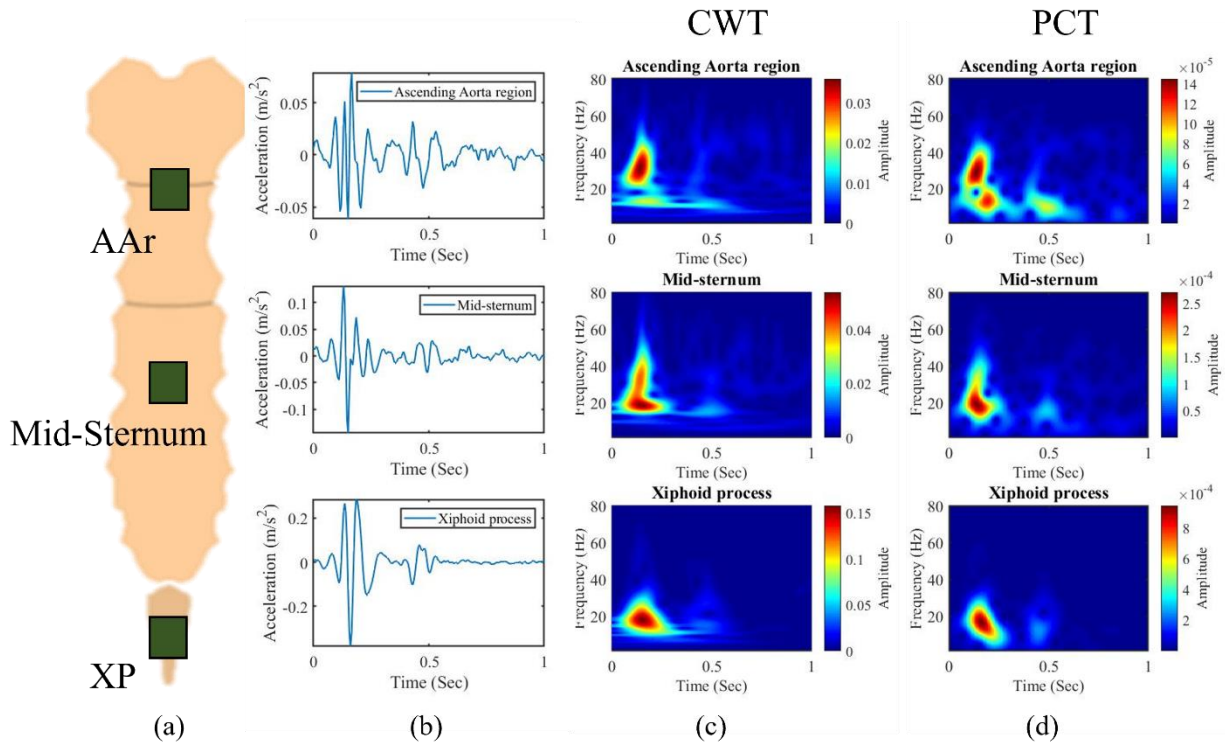


Figure 7: a) S-VCG locations. b) Average (25 heartbeats) dorso-ventral VCG collected from a subject in supine position during inhaled breath hold and corresponds to the locations shown in (a). c) Continuous wavelet transformation (Morse). d) Polynomial chirplet transformation.

plots were affected by spreading in the time domain at low frequencies as shown Figure 7 (c). Hence, only PCT based TFD representation was picked for further analysis.

2. TF Analysis

A custom algorithm was developed to extract both V1 and V2 peaks from the PCT plots. The workflow of the algorithm is detailed in Figure 8. Both time and frequency distribution in PCT showed a pseudo-gaussian distribution which can be seen in the 3D surface plot of Figure 8 (a). At first, only the time axis data was considered. MATLAB's findpk function was used to find the two highest peaks in the time plot. To remove false peak identification due to noise in the signal, a minimum time difference was set between two successive peaks. The value of the time

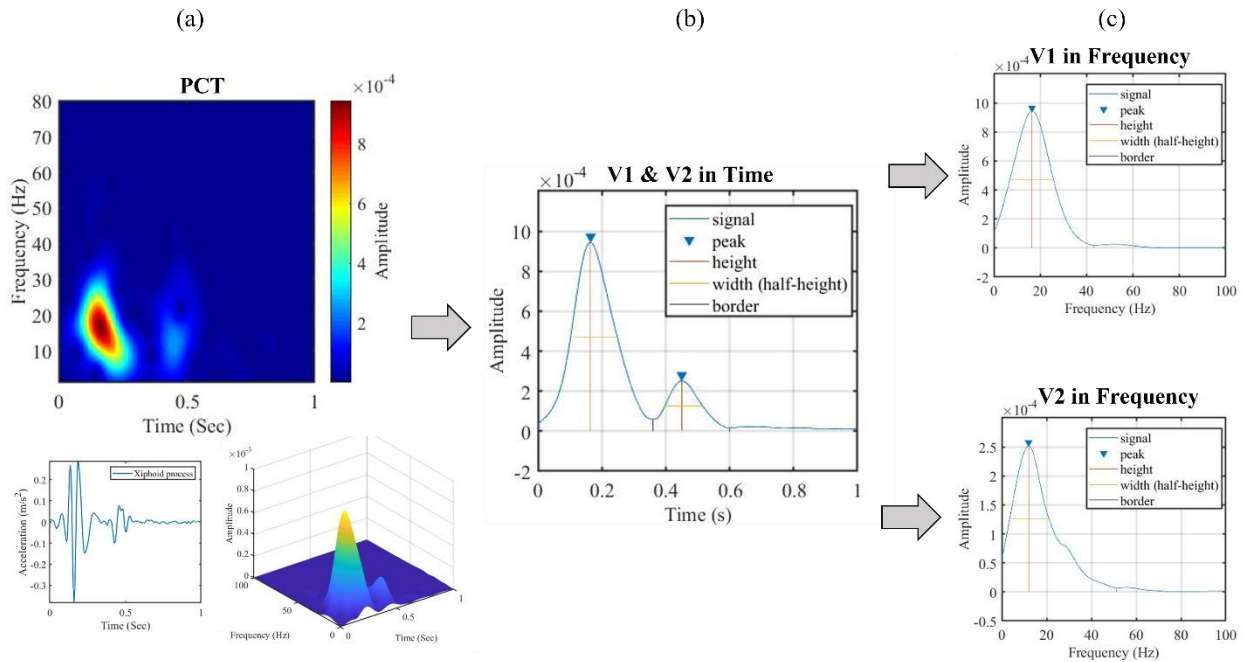


Figure 8: a) PCT of dorso-ventral VCG collected in supine position during inhaled breath hold at XP location (Top). Time domain signal (bottom left) and 3D surface plot (bottom right) is shown. b) V1 and V2 peak in time. c) V1 and V2 peak in frequency.

difference was taken from the LVET measurement detailed in Chapter III (B). From the 3D surface plot Figure 8 (a), it can be seen that the frequency profile of V1 covers the frequency profile of V2, and vice versa. Hence a direct frequency peak finding and split could not be done. To find the frequency profile of both V1 and V2, the time signal from Figure 8 (b) was first split. The splitting was performed at the minimum amplitude location between the peaks found in the time representation. The center frequency at the maximum peak location, and the corresponding frequency width from both separated V1 and V2 were then extracted as shown in Figure 8 (c).

E. Simulation of Cardiac Waveforms

To understand and validate the findings in the VCG signal, simple numerical based simulations were performed and the wave propagation path from the heart to the chest surface was analyzed. The COMSOL (COMSOL Multiphysics 5.6, COMSOL Inc.) software was used to perform the simulation task. The software uses finite element method and allows to study various

coupled physics phenomena. Within the software environment, the structural mechanics module was used to simulate the model.

1. Geometry and Materials

To reduce the complexity of the simulation while still maintaining results that can be correlated to the experimental VCG waveform, a simplified geometry approach was taken to design the chest and the organs within it. The geometry was designed as a 2D cross section on the transverse plane of the human body across the heart. The idea of the geometry was adopted from previous works on sound transmission in the chest [80, 81]. It is shown in Figure 9 (b). The circular chest geometry contained six domains representing different organs of the chest from the heart valves to the xiphoid process location. The geometry and the material parameters are shown in Table 4 below.

Table 4: Simulation geometry and material parameters

Domain	Geometry		Material Parameters		
	Element	Thickness (mm)	Lamé parameter λ (kPa)	Shear modulus μ (kPa)	Density ρ (kg/m ³)
1	Heart Valve	12.5 [82]	5.04	9	1000
2	Cardiac Muscle	27.5 [83]	6.86	12.25	1000 [84]
3	Soft Tissue	15	8.96	16	1000 [85]
4	Rib	2 [86]	50.28	89.6	1400[85]
5	Fat	2-8	.504	.9	900 [87]
6	Skin	2 [88]	14	25	1000[85]

Each of the domains were simulated as isotropic linear elastic materials. The Lamé parameter λ and the shear modulus μ values in the model were adapted from previous low frequency wave propagation speed study of the heart [89]. These were modified to find the relative elasticity for the rest of the organs. The path was designed without any lung region, as linear elasticity was inadequate to effectively model the behaviour of the lungs. This is further discussed in Chapter V. A layer of fat with varying thickness was placed before the final skin domain, representing Subject 1's fat mass loss over 6 weeks.

2. Physics

Any elastic solid can be parametrized by its density and elasticity. Any load originating from the heart valve area diffuses to the organs surrounding it. At each material boundary, due to

impedance mismatch, a portion of the original wave gets reflected. The propagation of the wave through each solid domain can be defined by the wave equation shown below.

$$\rho \frac{d^2 \mathbf{u}}{dt^2} = (\lambda + 2\mu) \nabla(\nabla \cdot \mathbf{u}) - \mu \nabla \times \nabla \times \mathbf{u} \quad (2)$$

Here ρ , λ , and μ are the material properties defined in Table 4. \mathbf{u} is the displacement of a particle from its equilibrium position. $\nabla \cdot \mathbf{u}$ represents volumetric deformation, and $\nabla \times \mathbf{u}$ represents shear deformation. The material properties define the pressure ($v_p = \sqrt{\lambda + 2\mu/\rho}$) and shear wave ($v_s = \sqrt{\mu/\rho}$) speeds in the material. The physics was implemented in COMSOL using the solid mechanics interface within the structural mechanics module. To reduce back reflection of the outward propagating waves, a perfectly matched layer was set up to absorb all outgoing waves. A low-reflecting boundary condition was also applied at the outer boundaries to further reduce modulation of the waveforms due to reflection.

3. *Input Load*

Each vibration source of the simulated VCG signal was assumed as an analytical function representing pulses of different amplitude. The amplitude difference was adopted from the results of the VCG SNR measurement shown in Chapter III A. Two pulses at 150 ms and 500 ms were inputted to the model as shown in Figure 9 (a). They correspond to the V1 and V2 timing of VCG. The pulses were inputted using either the prescribed displacement node or the body load node in COMSOL, depending on the performed analysis.

4. *Study and Mesh*

The simulation performed two different types of analysis. At first, the effect of fat layer and circumference reduction was studied. During this step, the model input was set up as a prescribed displacement of two pulses as shown in Figure 9 (a). This was done to eliminate any vibration of the input domain that might lead to a noisy output signal. A second study was performed to analyze the effect of cardiac contractility on VCG waveforms. During this study, the same input function in Figure 9 (a) was inputted using the body load node, to include the effect of the vibration of the input domain itself on the acquired result. A user-defined mesh was implemented and optimized to minimize computational intensity with about 15 mesh nodes per

wavelength. Due to the simplicity of the model, the software was able to handle computation with ease (approximately 20 minutes per one second study). A time-dependent study for one second was performed covering an approximate time interval of a full cardiac cycle. The output of the model was probed below the skin layer.

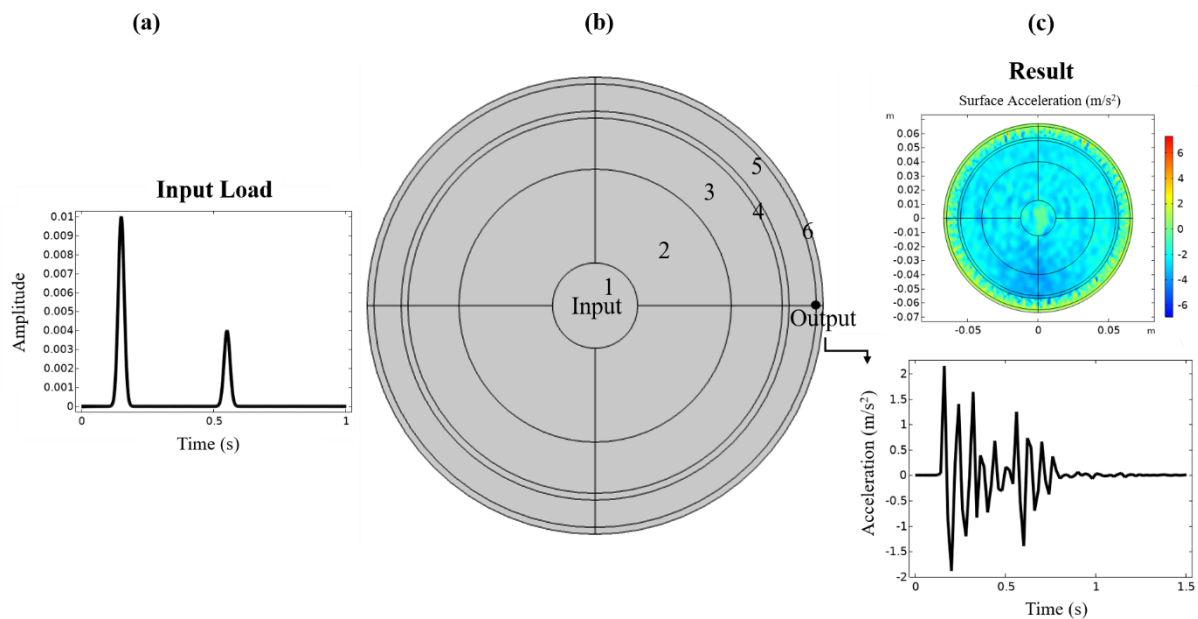


Figure 9: (a) Input V1 and V2 pulse load. (b) Geometry with six different domains. Load was inputted in domain 1. (c) (Top) Surface plot of Acceleration propagation during the simulation. (Bottom) Acceleration value at Output node (skin layer) representing a synthetic VCG signal.

IV. RESULTS

The Results chapter describes the findings of the analysis described in Chapter III, from the tests performed in Chapter II.

A. Signal-to-Noise ratio

1. SNR and Sensor Placement

The relative SNR for the all the measurement locations for different tests are given in the appendix (Chapter VII A). For the subjects at rest, the average V1 showed 64% higher SNR than V2. It increased to 81% during LLV breath hold test, and to 89% during HLV breath hold. Table 5 shows the Average SNR for all subjects at different positions on the chest.

Table 5: Average SNR for all subjects during the different tests performed

Chest positions	V1 SNR				V2 SNR			
	Rest	HLV	LLV	Average	Rest	HLV	LLV	Average
XP	3.18	7.14	3.83	4.72	2.31	4.54	2.23	3.03
TV	4.42	7.41	4.52	5.45	2.38	3.25	1.91	2.51
MV	4.44	6.68	4.08	5.07	1.82	2.76	1.81	2.13
AV	3.19	2.92	2.96	3.02	2.14	1.69	2.14	1.99
Mid-S	2.68	3.48	3.00	3.05	1.74	1.93	1.8	1.82
PV	2.49	2.96	3.08	2.84	1.74	1.47	1.8	1.67
AAr	2.10	2.33	2.84	2.42	1.58	1.64	1.77	1.66

For measuring V1, the TV location showed the best SNR metric at 5.45, with the MV position at second with 5.07, and the XP location at third with 4.72. For V2 measurement, the XP location showed the highest SNR metric of 3.03, with TV at 2.51, MV at 2.13. In these three positions, HLV tests always showed the best SNR, and opposite was observed during LLV tests. The data verifies that the XP is still the overall best position for collecting VCG signal, however the TV location would be ideal if only V1 is of interest. It was hypothesized that that the AV, Mid-Sternum, and the PV locations would provide better V2 SNR than other locations, due to their proximity to the aortic valve. While it was true for some cases, the opposite was observed for most of the tests. It can be attributed to the overall low-quality signal gathered from these locations.

From the results, it is suggested that the relative RMS for V1 and V2 should be at least above two to properly identify the fiducial points when using the system at home, or in a clinical setting.

2. SNR During Weight Loss

Table 6 shows the relative SNR results for the weight loss participant for the three best locations discussed in the previous step. V1 SNR generally improved during all tests as the subject underwent weight loss and strength training over the six weeks.

Table 6: V1 and V2 SNR at XP, TV, and MV for Subject 1. Corrupted data due to system failure shown as empty cells

Test	Test type	V1 SNR			V2 SNR			V1 Change (Average of all locations)	V2 Change
		XP	TV	MV	XP	TV	MV		
Week 1	Rest	2.42	3.02	3.80	1.60	1.94	1.43	N/A	N/A
	HLV	7.00	6.21	7.17	5.59	2.07	2.72	N/A	N/A
	LLV	3.96	4.17	3.84	2.10	1.67	1.70	N/A	N/A
Week 3	Rest	3.29	3.77	4.53	1.70	1.49	1.46	25.4%	-6.4%
	HLV		7.96	7.11		2.51	3.05	10.9%	-19.7%
	LLV		4.47	4.07		1.34	1.46	7.0%	-23.2%
Week 6	Rest	3.51	5.31	6.13	2.06	2.05	1.92	29.0%	29.7%
	HLV	12.17	9.22	7.56	3.74	2.24	3.49	28.1%	13.5%
	LLV	4.72	5.05	6.03	1.67	1.75	1.67	23.3%	21.2%

The measured SNR is visualized in Figure 10 against the participant's BMI. At the end of the six weeks, V1 SNR showed improvement of 29% during rest, 28.1% during HLV breath hold, and 23.3% during LLV breath hold tests. The participant's physiological parameters were shown in Table 3. Over the six weeks, the participant's chest circumference reduced by 8.3 cm, body fat percentage dropped by 4.93%, the participant lost 11.2 kg of (9.6 kg fat mass) overall weight, all of which could contribute to the improvements of V1 SNR. The observed results are further discussed in the next chapter. The trend in SNR improvement was less clear for V2, as the relative RMS value was below two for most of the tests.

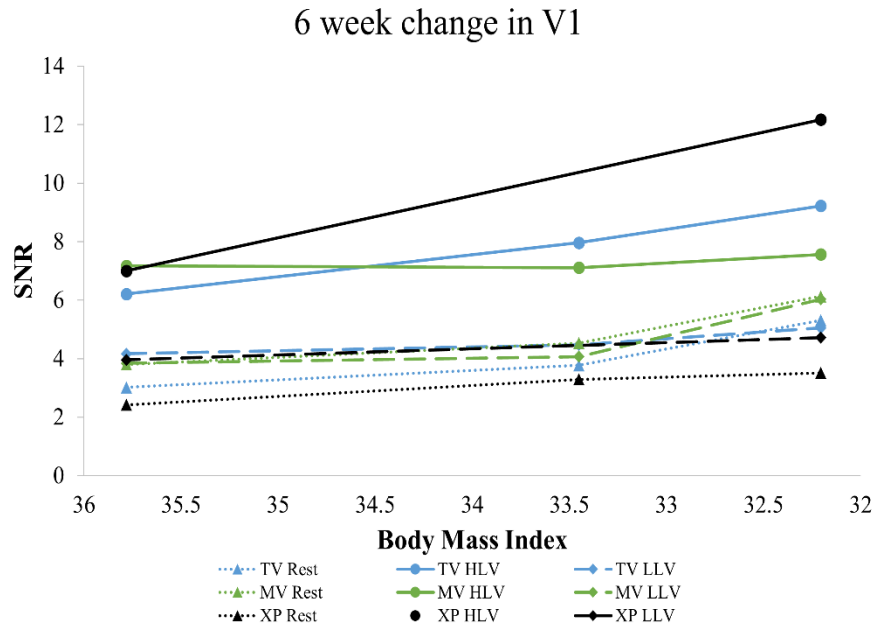


Figure 10: V1 SNR from three Sensor locations (TV, XP, and MV) for all the tests are plotted against the subject's BMI changes over 6 weeks.

B. Cardiac Timing

IVCP, LVET, and IVRP from all subjects were extracted and shown in the appendix (Chapter VII B). The average results per position for all the subjects are discussed here. During rest, the highest IVCP was reported by the XP and MV positions at 54 ms and 52 ms with a standard deviation (SD) of 19 ms and 26 ms respectively. The lowest IVCP values were reported from the PV, AV, and the TV location at 37 ms. However, the lowest values of IVCP were still within the SD of XP and MV. The average rest LVET value for all the locations was found to be 320 ms, with a SD of 20 ms. The LVET measured from each of the locations were also within the SD range. Similar observations were found for IVRP at rest, with the XP location being the highest (85 ms) and the PV location reporting the lowest IVRP value (58 ms).

Figure 11 demonstrates IVCP, LVET, and IVRP in a bar plot for the different chest locations. During each of the different type of tests (Rest, HLV, or LLV), all locations showed comparable values that are within the error limit of each other. Hence, cardiac timings could be acquired from each of the tested locations in the chest when the system is deployed for at home

use. It was reported previously that breath holding affects the cardiac cycle [47, 59, 90]. A change in cardiac timing was found as shown in Figure 11. However, no clear trend was observed. For the

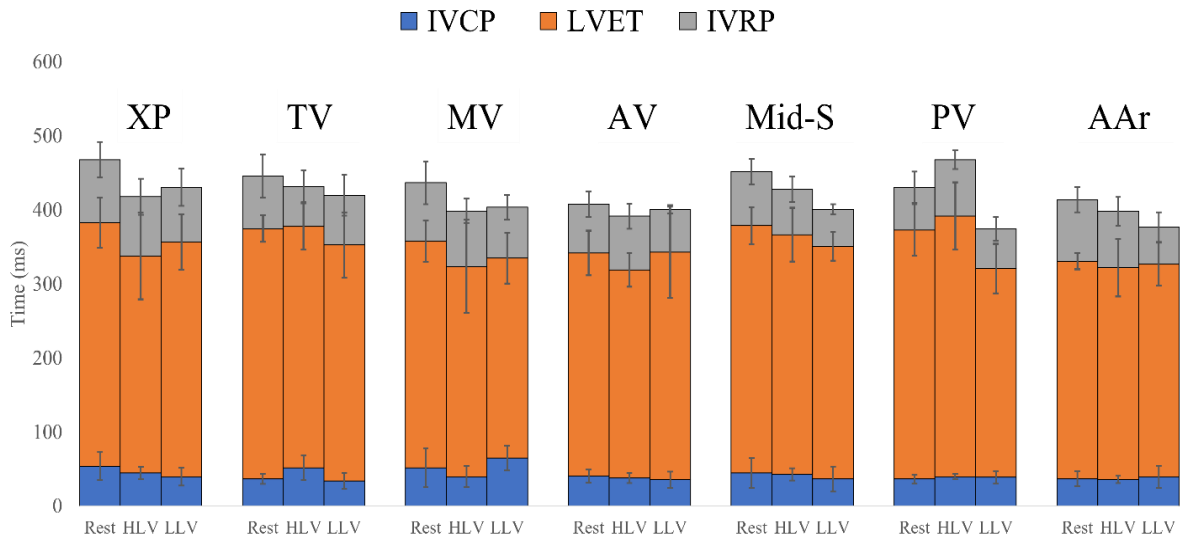


Figure 11: The bar plot represents IVCP (in blue), LVET (in orange), and IVRP (grey) for all subjects at each location of the chest. The SD is plotted as vertical error bars.

weight loss participant, the cardiac timing from each location acquired at week six remained within the SD of the values acquired during week 1. Hence, no change in cardiac timing was observed for the weight loss participant.

C. Dominant Frequency

The dominant frequencies at each sensor position were extracted for all the tests using DFT and Pwelch method. All locations on the chest reported similar frequency metrics, and three dominant frequencies were found in the VCG waveform. Table 7 shows the frequencies found per subject as f_1 , f_2 , and f_3 . The signal contained a dominant frequency at 10 Hz during most of the tests, while a lower frequency at 3.125 Hz was also evident. Another dominant frequency was found around 25 Hz. For some tests, this was indistinguishable with another frequency found around 35 Hz. A higher frequency value between 45 and 50 Hz was also found and is assumed to be a harmonic of the frequency located at 25 Hz [16]. No significant change in the dominant frequencies from wight loss participant was observed over the six weeks.

Table 7: Average dominant frequencies found for each subject

Subject	f 1	f 2	f 3
1	10.53 Hz	26.14 Hz	45.63 Hz
2	8.618 Hz	23.17 Hz	33.4 Hz
3	6.41 Hz	29.84 Hz	37.26 Hz

D. V1 and V2 Peak

VCG waveforms corresponding to each heartbeat were first converted to its PCT representation. The algorithm described in Chapter III D was then applied to split the waveforms in time and frequency. Analyzing it gave a measure of the time and frequency location and widths of V1 and V2. The results specific to each individual subject are given in the appendix (Chapter VII C). No trend in the time and frequency location and widths of V1 and V2 was observed for the subject who underwent weight loss. The average results for all the subjects are discussed here.

1. Time

The time distribution of V1 and V2 were extracted and shown in Table 8. All the sensor positions reported comparable V1 and V2 peak time during rest at an average of 175 ms and 539 ms respectively. However, during breath hold, both V1 and V2 peak time reduced. Both HLV and LLV breath hold results were comparable at around 155 ms for V1, and at 496 ms for V2. This establishes the effect of breath holding on V1 and V2 peak occurrence.

Table 8: Location of V1 and V2 peaks in time

Chest positions	V1 peak time (ms)			V2 peak time (ms)		
	Rest	HLV	LLV	Rest	HLV	LLV
XP	148	160	159	541	468	519
TV	172	140	149	537	495	484
MV	200	141	153	538	481	529
AV	188	166	191	505	481	510
Mid-S	221	141	146	496	517	471
PV	160	172	157	583	503	514
AAr	142	157	149	578	469	485

Amplitude concentration around center time and frequency for both V1 and V2 showed a gaussian distribution. Hence the full width half maximum (FWHM) values were extracted for each of V1 and V2 peak, in time and frequency domain. The FWHM of each time peak are reported in Table 9. The relative differences based on the sensor positions were within the average SD. However, HLV breath hold tests showed a significantly low V1 peak width at an average 125 ms than rest (144 ms) and LLV (139 ms) tests. The V2 peak width was comparable to V1, and also showed a lower width during HLV (132 ms), than rest (147 ms) and LLV (152 ms) tests.

Table 9: V1 and V2 peak widths in time

Chest positions	V1 peak width (ms)			V2 peak width (ms)		
	Rest	HLV	LLV	Rest	HLV	LLV
XP	136	129	163	134	105	174
TV	146	131	120	151	126	129
MV	150	114	121	153	128	154
AV	174	140	156	158	104	179
Mid-S	122	113	149	150	177	130
PV	145	117	120	155	172	147
AAr	134	131	145	130	119	153

2. Frequency

The V1 and V2 center frequencies are reported in Table 10. Averaging the values found from each location, V1 center frequency was found to be 15.6 Hz.

Table 10: Center frequency of V1 and V2

Chest positions	V1 Center Frequency (Hz)			V2 Center Frequency (Hz)		
	Rest	HLV	LLV	Rest	HLV	LLV
XP	10.9	17.4	11.6	11.3	18.7	10.9
TV	15.4	15.3	14.3	9.7	17.3	12.8
MV	12.1	14.8	12.8	9.7	14.6	9.1
AV	23.3	22.5	13.7	10.2	11.0	12.8
Mid-S	14.2	21.2	16.4	12.3	21.6	10.6
PV	13.5	27.0	18.0	17.3	9.1	13.4
AAr	19.7	29.1	20.1	14.6	18.8	12.7

While this increased to 21.04 Hz during HLV, it slightly decreased to 15.3 Hz during LLV. This trend was also observed for V2. Center frequency during rest was at 12.2 Hz. It increased to 15.9

Hz during HLV and decreased to 11.8 Hz during LLV. High location variability in the data was found. This was attributed to the noise in the measured signal, at positions away from the heart.

FWHM values were extracted for each of V1 and V2 peak in the frequency domain. The results are shown in Table 11. Both peak 1 and 2 frequency widths were around 16 Hz during rest, and increased to around 20 Hz during HLV test. LLV tests showed frequency widths of 17 Hz for both V1 and V2.

Table 11: Frequency widths of V1 and V2

Chest positions	V1 Frequency Width (Hz)			V2 Frequency Width (Hz)		
	Rest	HLV	LLV	Rest	HLV	LLV
XP	15.9	15.4	14.6	16.4	24.3	18.1
TV	13.7	23.0	23.0	14.1	23.9	15.6
MV	15.5	18.7	16.8	14.4	17.7	16.6
AV	12.5	23.1	14.0	22.2	24.1	15.9
Mid-S	16.4	21.6	20.9	16.9	13.5	16.5
PV	16.5	18.5	16.0	12.7	19.8	17.3
AAr	21.5	17.1	14.6	18.5	17.4	19.6

E. Simulated VCG

To verify the findings of the SNR changes for the weight loss participant, a simple numerical model was built in COMSOL to represent the wave propagation path from the heart valves to the VCG measurement locations. The geometry of the model was shown in Figure 9, while the material properties used for each domain was given in Table 4. To test the improvements in SNR shown at the beginning of this Chapter, domain 5 thickness was changed between 2 mm and 8 mm, representing the subject's fat mass loss, and reduction in chest circumference. The results are plotted in Figure 12. As the fat layer thickness decreased from 8mm to 2mm (fat percentage reduced by 12.7%), the V1 peak RMS value improved by 90% from 1.24 to 2.35, hence predicting a connection between body composition and VCG signal amplitude. The RMS values were extracted with the method shown in Chapter III A. V2 amplitude did not show the same trend. This was attributed to the increased oscillations of the skin layer due an increased thickness of the softer fat layer underneath, and back reflections modulating the lower V2 amplitude peak.

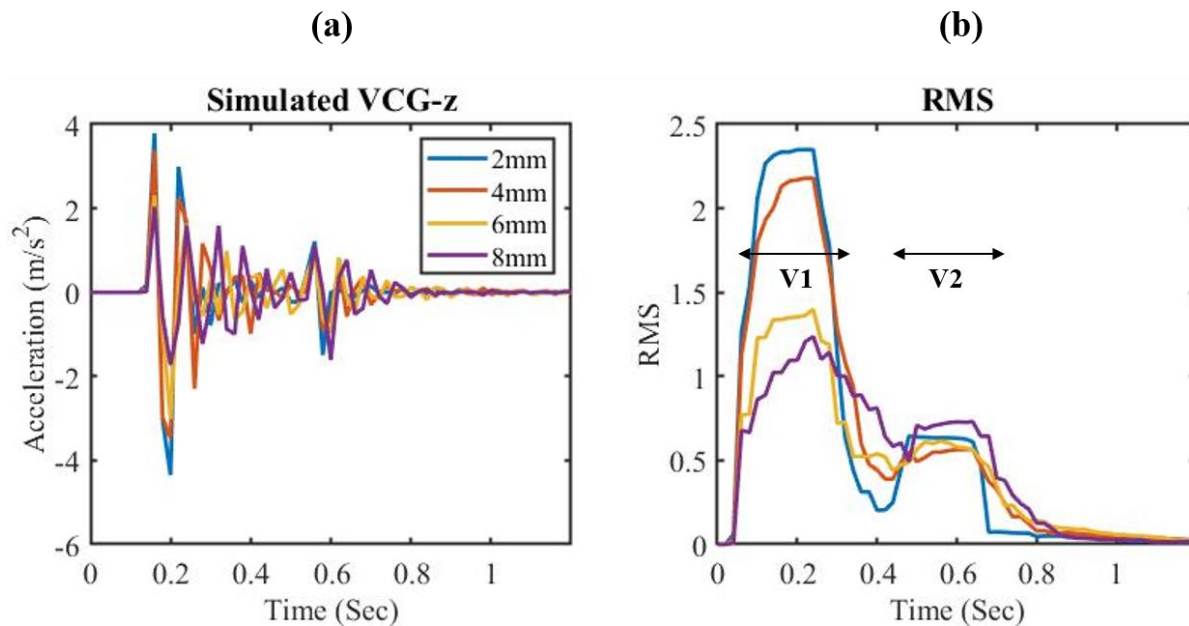


Figure 12: (a) Simulated dorso-ventral axis VCG plotted for different fat layer thickness (domain 5). (b) RMS values corresponding to the different VCG waveform.

Effect of exercise and cardiac contractility on VCG SNR was also investigated through the model. Cardiac compliance increases [91] due to exercising. During systole, a more contractile heart (for example, an athlete's heart) ejects a greater stroke volume through the valves. This leads to a greater pressure differential across the heart valves which is hypothesized to produce a greater vibrational pulse, and as a result, a greater amplitude in the VCG signal. This was emulated by changing the material stiffness parameter of the input and the cardiac muscle domain. The results are shown in Figure 13. The model input was changed to a body load representing a force instead of previously used prescribed displacement to identify the effect of the material parameter change in the input domain. However, this also resulted in spurious oscillations in the simulated VCG signals. The results still showed an expected trend.

As the elastic modulus of the input and the cardiac muscle domain was decreased from 10 kPa to 1 kPa, the V1 amplitude of the synthetic VCG captured at the skin domain increased by almost 90% as shown in Figure 13 (b). V2 amplitude also showed this trend.

Hence, both body fat reduction and increased heart contractility was attributed to an increased V1 amplitude and SNR of the VCG signal.

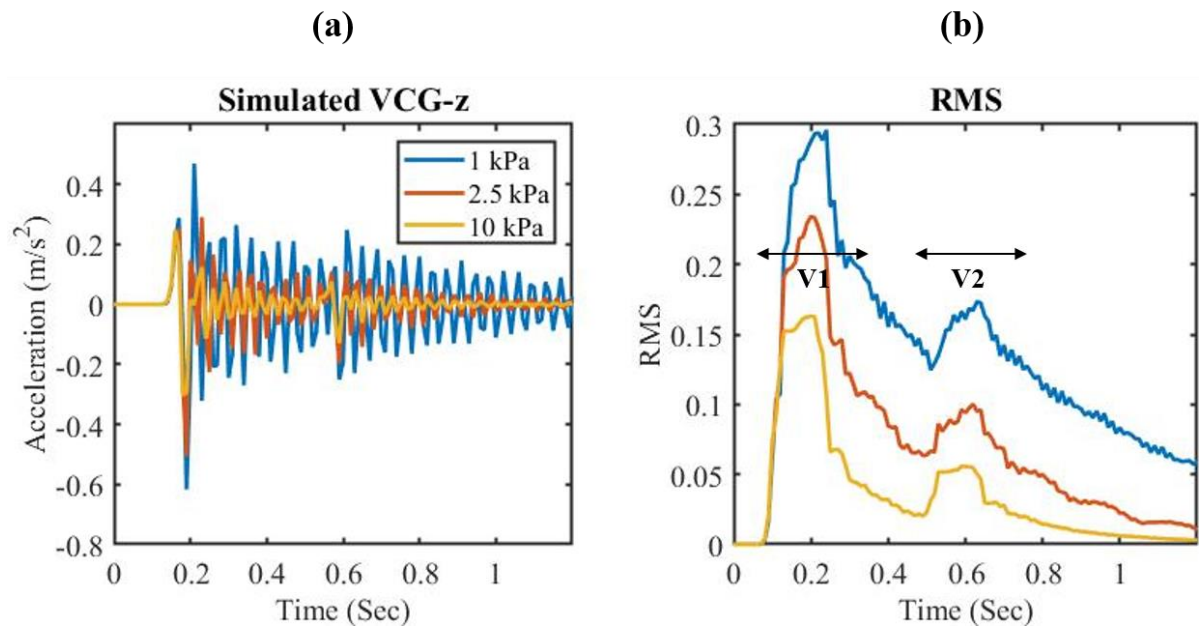


Figure 13: (a) Simulated dorso-ventral axis VCG plotted for different input domain elasticity. (b) RMS values corresponding to the different VCG waveform

V. DISCUSSION

V1 SNR showed about 25% improvement after subject 1 performed six weeks of weight loss routine and 180 minutes per week strength training exercise. The exercise was done to supplement the participant's weight loss goal, and to maintain the BMR required to lose the desired weight. V1 relates to the cardiac event of aortic valve opening and the beginning of the ventricular systole. The morphological changes in the chest that could potentially lead to better SNR were identified as three main aspects: 1) Reduced body fat mass, 2) Decreased chest circumference, and 3) Increased ventricular contractility and ventricular thickening due to exercising. The implications of each of them on the acquired VCG signal are discussed below.

Over the six weeks, the participant had a reduction of 9.6 kg subcutaneous and visceral fat mass, and an 8.3 cm reduction of chest circumference. VCG waves are the localized vibrations of the heart acquired at the chest. Any wave travelling through multiple materials experience reflection, refraction, and damping due to discontinuities and inherent material properties. Hence, a reduction in the fat layer could lead to less damping in the path of the VCG waveform, leading to a higher signal amplitude at the skin surface. The wave propagation simulation results also showed this effect. An increase in synthetic VCG V1 signal amplitude was found as the fat layer thickness and chest circumference were reduced. However, any concrete proof to connect fat mass reduction to VCG will need addition metrics such as echocardiogram images of the subject at different times during the period of the weight loss. Collecting echocardiogram images requires proper medical equipment and appropriate lab setting. It was out of scope for the project.

The effect of regular exercising on cardiac health has been explored in literature previously. Cardiac compliance increases [91], and stiffness decreases [92] due to exercising. As the heart is a muscle, increased physical activity has shown to be associated with an increase in ventricular thickness [93]. A stronger heart pumps more blood per cardiac cycle. The blood pressure across the valves along with valve elasticity and mass gives rise to the vibration at the valves [94]. The effect of cardiac contractility was emulated on the synthetic VCG signal, and increased contractility showed better VCG signal amplitude. Hence all three aspects could lead to a better SNR of cardiac vibrations.

However, increased pressure difference across the heart valves also leads to an increase of the frequency of vibration of the valves [95]. VCG V1 peak has been assumed to be a direct manifestation of vibrations originating at the cardiac valves and hence an increase in V1 peak frequency after six weeks could have further justified the assumed physiological changes. No such trend in the frequency content of the VCG signal was observed from the weight loss participant over the six weeks. Moreover, the effect of 180-minute exercise per week might have been inadequate to result in ventricular thickening. For example, an 8 week 2 hours/day, 5days/week high-intensity treadmill exercise on rats showed 20-30% thickening of cardiac muscle cells [96]. The results show that a much higher intensity of workout might have been required for ventricular thickening of subject 1. Hence, fat mass and chest circumference reduction are assumed to be the biggest modulator of the improved VCG SNR, with increased cardiac contractility also affecting the signal. Ventricular thickening is assumed to be the least probable cause of VCG SNR improvement.

The cardiac timing intervals such as IVCP, LVET, and IVRP did not vary between measurement positions. The collected results were deemed reasonable as all sensor positions recorded the same cardiac cycle, and ideally should report the same values.

While the dominant frequency results acquired through DFT and Pwelch allowed to easily create a frequency representation of the signal and match the acquired results with previous works, it did not provide any valuable information that could be correlated to the cardiac beating process. The frequency domain results further motivated the development of a TFD representation of the cardiac signal and the V1 and V2 peak and width detection algorithm. While PCT showed better amplitude concentration for V1 and V2 than CWT, it is still not ideal for studying multi-frequency component signals. Any additional VCG signal component around V1 and V2 could not be identified if those components were within the FWHM of V1 and V2. This would explain why the assumed ascending aorta component of the VCG signal was not identifiable during the analysis. According to the cardiac cycle, the vibration in the aorta would occur right after the aortic valve opening, and if it arrives at the sensor within the FWHM of the V1 peak, it would be superimposed by the larger AO event. Hence, a more robust multi-component signal analysis tool should be used for future TFD studies of the VCG signal.

Using the PCT method, both V1 and V2 peaks showed similar time and frequency contents. While the V1 peak frequency results match with previous works, the results differ on V2 frequency profile [16]. This can be attributed to the method used to extract both peaks. Pulse dispersion analysis could be done to further analyze the peak widening of V1 and V2 at different sensor locations.

Several shortcomings of the performed study have been recognized. Firstly, to properly identify the biological and physiological implications of the study, a much larger population data collection must be done. However, it was not feasible due to restrictions placed by the Covid-19 pandemic. Although it was compensated through simulation work, no concrete proof was extracted from the results of the simulation. This is due to the oversimplification of the human body during the simulation performed. Biological tissues exhibit complex stress-strain relationships, and hence approximating organs with linear elastic materials in simulation lead to an inadequate representation of the human body. For example, soft tissues are consisted of elastin and collagen fiber families that give rise to directional stress-strain relationships [97]. Hence a proper viscoelastic [98], or a hyperelastic material model is required [97] to understand their behaviour. The lung has been shown to be a prime modulator of VCG waveform amplitude [46, 47]. However, modeling vibrational wave propagation in the lung would required the use of Biot theory of poroviscoelasticity, or the effective medium theory [99]. While a more detailed simulation might have been able to provide more insight on the functioning of the heart, cardiac simulations are still a cumbersome task, and require many assumptions because of the interconnected dependencies of the human body.

Lastly, while only the dorso-ventral axis VCG was studied in this thesis, simultaneous analysis of the other axes would allow to study the affect of ventricular twist on sensor position and respiration modulation of VCG signals at different positions.

VI. CONCLUSION

A system capable of wireless cardiac monitoring from multiple positions on the chest was developed in the lab. The system is cost-effective, and easily usable to provide cardiac assessment at home. VCG waves collected at different positions in the chest were studied. Location specific amplitude modulation was observed and identified through V1 and V2 SNR. The results verified the previous claims of the xiphoid process being the best location for collecting the overall VCG signal. However, if only V1 is of interest, the tricuspid valve auscultation showed the best V1 amplitude. For any system built to acquire VCG waveforms, a minimum V2 SNR metric of two should be ensured while finding the sensor location for at home or clinical use. Measuring a subject undergoing weight loss showed approximately 25% VCG V1 SNR improvement as the subject's body fat percentage reduced by almost 5%, chest circumference reduced by approximately 7%, and as BMI reduced by 10%. However, improved heart functions such as increased ventricular contractility due to exercising could also be a modulator of the VCG waveforms. All valve positions were able to pick up cardiac timing intervals. Both V1 and V2 peaks showed similar frequency content when studied with PCT. Morphological frequency modulation was not observed. A larger population study is required to further verify the findings of the current thesis.

VII. APPENDIX

All the results from each of the subject's tests are given below.

A. SNR

Subject	Test type	Sensor locations								
		MV	Mid-S	AAr	XP	PV	AV	TV		
V1 SNR	1 W1	Rest	3.80	2.04	1.68	2.42	1.71	2.14	3.02	
		HLV	7.17	2.83	1.59	7.00	2.01	1.77	6.21	
		LLV	3.84	2.55	2.52	3.96	2.93	1.78	4.17	
	1 W3	Rest	4.53	2.61	2.19	3.29	2.17	2.79	3.77	
		HLV	7.11	2.53			2.60	2.67	7.96	
		LLV	4.07	2.44			2.76	2.08	4.47	
	1 W6	Rest	6.13	2.45	2.63	3.51	2.44	2.83	5.31	
		HLV	7.56	3.40	2.87	12.17	3.91	3.95	9.22	
		LLV	6.03	3.29	2.39	4.72	3.16	2.38	5.05	
	2	Rest	3.82	3.75	1.90		4.12	5.94	6.59	
		HLV	4.14	3.55	2.09	8.42	3.19	3.01	7.07	
		LLV	3.26	4.12	4.56	3.01	4.75	6.73	5.72	
	3	Rest	3.92	2.53		3.52	2.02	2.23	3.40	
		HLV	7.43	5.09	2.78	0.99	3.09	3.22	6.60	
		LLV	3.21	2.59	1.91	3.66	1.79	1.83	3.20	
	V2 SNR	1 W1	Rest	1.43	1.40	1.40	1.60	1.93	1.18	1.94
			HLV	2.72	1.39	1.36	5.59	1.26	1.73	2.07
			LLV	1.36	1.34	1.75	2.10	1.95	2.09	1.67
1 W3		Rest	1.46	1.29	1.49	1.70	1.46	1.44	1.49	
		HLV	3.05	1.22			1.69	1.65	2.51	
		LLV	1.46	1.17			1.49	1.49	1.69	
1 W6		Rest	1.92	1.72	2.19	2.06	1.58	2.59	2.05	
		HLV	3.49	1.37	1.71	3.74	1.55	1.65	2.24	
		LLV	1.67	2.35	1.92	1.67	2.12	1.64	1.75	
2		Rest	1.84	2.16	1.24		2.23	4.21	3.18	
		HLV	2.18	3.12	1.87	8.28	1.35	2.07	5.42	
		LLV	2.03	2.72	2.23	3.21	1.95	4.32	2.80	
3		Rest	2.42	2.12		3.90	1.49	1.30	3.22	
		HLV	2.38	2.52	1.60	0.56	1.53	1.37	4.02	
		LLV	2.52	1.45	1.16	1.95	1.46	1.18	1.64	

B. IVCP, LVET, and IVRP

Cardiac timings (ms)			Sensor locations							
Subject	Test type		MV	Mid-S	AAr	XP	PV	AV	TV	
IVCP	1 W1	Rest	20	35	35	55	35	40	30	
		HLV	50	45	40	45	40	35	55	
		LLV	70	65	55	55	45	30	25	
	1 W3	Rest	90	80	30	80	35	50	40	
		HLV	50	50			40	45	75	
		LLV	80	40			50	45	30	
	1 W6	Rest	60	30	30	40	30	30	45	
		HLV	50	50	40	55	45	45	55	
		LLV	45	25	50	40	35	50	40	
	2	Rest	50	35	35		40	35	30	
		HLV	20	30	30	35	35	30	30	
		LLV	80	25	25	25	35	25	25	
	3	Rest	40	45	55	40	45	50	40	
		HLV	30	40	35	45	40	35	45	
		LLV	50	30	30	40	30	30	50	
	LVET	1 W1	Rest	330	310	290	280	315	330	310
			HLV	345	350	345	345	380	285	355
			LLV	260	305	260	280	260	375	355
1 W3		Rest		310	310	355	370	290	330	
		HLV	225		265	200	340	250	275	
		LLV	255	320	335	365	325	280	320	
1 W6		Rest	285	370	290	330	295	265	350	
		HLV	210	340	250	275	350		345	
		LLV	320	325	280	320	285	370	350	
2		Rest	280	335	285		325	320	345	
		HLV	335	335	305	335	405	305	335	
		LLV	285	335	290	340	300	270	325	
3		Rest	330	345		350	375		355	
		HLV	305	270	265	310	285	285	320	
		LLV	230	285	270	280	240	240	245	
IVRP		1 W1	Rest	80	90	105	80	70	55	55
			HLV	95	60	60	80	75	80	45
			LLV	80	45	60	80	70	60	55
	1 W3	Rest		75	85	65	80	65	120	
		HLV	90		100	115	85	90	90	
		LLV	80	60	65	65	50	60	115	
	1 W6	Rest	110	80	65	120	70	90	55	
		HLV	65	85	90	90	85		35	
		LLV	70	50	60	115	70	55	50	
	2	Rest	40	45	75	0	35	55	50	
		HLV	65	45	55	55	80	70	55	
		LLV	40	45	50	50	35	65	50	
	3	Rest	85	75		75	35		75	
		HLV	60	55	75	60	55	50	45	
		LLV	75		15	60	45	50	65	

C. PCT

Rest	Subject	Sensor locations						
		MV	Mid-S	AAR	XP	PV	AV	TV
V1 Time Location (ms)	1 W1	150	235	230	195	225	215	135
	1 W3	155	135	125	190	230	130	150
	1 W6	140	125	230	160	255	165	140
	2	165	125	215		135	145	160
	3	130	240	0	205	260	145	125
V2 Time Location (ms)	1 W1	595	585	535	525	490	565	585
	1 W3	425	585	470	470	500	650	580
	1 W6	555	550	490	535	490	605	570
	2	645	480	655		490	495	660
	3	485	485		490	510	600	495
V1 Time Width (ms)	1 W1	140	125	185	150	105	220	155
	1 W3	160	235	90	190	135	75	160
	1 W6	140	100	155	200	135	150	135
	2	110	115	170		95	120	125
	3	130	155		155	140	160	95
V2 Time Width (ms)	1 W1	120	225	175	140	135	100	140
	1 W3	155	140	130	180	200	185	125
	1 W6	130	180	205	210	180	215	135
	2	125	100	100		110	90	135
	3	140	110		100	125	185	115
V1 Center Frequency (Hz)	1 W1	11.6	7.0	12.1	11.8	10.8	12.4	15.4
	1 W3	10.8	12.2	26.1	10.6	10.2	29.7	11.9
	1 W6	12.7	17.3	10.8	13.1	8.6	11.4	13.1
	2	15.4	28.5	29.7		29.8	34.6	13.5
	3	9.9	6.1		8.0	8.0	28.4	22.8
V2 Center Frequency (Hz)	1 W1	7.5	12.5	10.7	9.6	14.2	10.7	10.1
	1 W3	10.4	4.6	13.4	10.7	13.3	5.8	6.0
	1 W6	8.2	10.9	11.5	6.5	11.8	6.6	8.2
	2	7.7	26.7	22.7		39.5	21.7	7.6
	3	14.6	7.1		18.5	7.8	6.5	16.6
V1 Frequency Width (Hz)	1 W1	14.5	8.8	15.2	16.8	18.0	16.9	25.2
	1 W3	14.1	17.4	20.0	14.1	16.5	20.0	19.9
	1 W6	16.8	6.2	8.5	3.8	7.2	9.2	17.3
	2	20.1	19.5	18.3		25.3	20.8	23.0
	3	14.1	16.7		15.3	15.0	15.7	22.2
V2 Frequency Width (Hz)	1 W1	9.1	9.5	16.6	12.8	17.9	6.7	17.9
	1 W3	17.3	10.2	12.6	30.1	9.7	5.9	16.2
	1 W6	16.1	19.8	14.9	17.7	19.9	10.6	13.6
	2	19.2	21.3	13.5		24.2	25.1	14.2
	3	20.0	9.9		28.2	12.9	15.3	30.4

HLV	Subject	Sensor locations						
		MV	Mid-S	AAr	XP	PV	AV	TV
V1 Time Location (ms)	1 W1	175	150	140	215	140	150	160
	1 W3					140	145	175
	1 W6	175	140	135	165	135	205	160
	2	150	130	135	145	135	190	140
	3	140	140	155	140	155	170	150
V2 Time Location (ms)	1 W1	495	545	490	530	425	475	470
	1 W3					635	470	480
	1 W6	425	490	485	450	520	520	430
	2	490	490	485	490	540	510	490
	3	460	455	465	455	465	540	475
V1 Time Width (ms)	1 W1	160	165	155	190	110	90	140
	1 W3					125	115	145
	1 W6	130	145	85	140	105	160	125
	2	115	110	75	115	125	95	125
	3	110	105	140	115	100	125	120
V2 Time Width (ms)	1 W1	115	115	120	115	150	210	160
	1 W3					190	165	140
	1 W6	110	175	195	115	210	195	100
	2	80	100	70	95	240	150	90
	3	115	115	125	90	95	140	105
V1 Center Frequency (Hz)	1 W1	9.7	12.3	27.2	11.1	25.9	31.1	13.4
	1 W3					29.9	26.8	12.2
	1 W6	11.4	19.0	28.8	16.4	24.8	15.1	14.4
	2	10.3	26.7	32.4	15.6	28.9	12.0	12.2
	3	28.0	26.8	28.0	26.4	25.5	27.4	24.5
V2 Center Frequency (Hz)	1 W1	12.6	19.4	14.8	13.2	10.3	12.8	7.9
	1 W3					6.4	13.5	12.0
	1 W6	17.9	15.4	10.0	12.1	11.8	6.6	8.2
	2	17.9	29.4	28.9	25.2	8.9	13.4	25.6
	3	9.9	22.3	21.7	24.3	8.1	8.8	32.9
V1 Frequency Width (Hz)	1 W1	12.1	14.9	22.8	23.1	26.3	19.3	20.1
	1 W3					17.0	9.9	16.3
	1 W6	13.3	26.8	20.3	18.9	24.0	26.5	18.2
	2	18.0	23.2	11.7	24.3	22.6	19.2	15.8
	3	18.2	27.0	20.0	25.9	18.0	17.6	15.2
V2 Frequency Width (Hz)	1 W1	25.9	17.5	24.9	18.3	17.1	16.5	7.8
	1 W3					7.6	12.8	14.7
	1 W6	21.0	18.4	17.2	18.2	17.5	28.9	22.8
	2	22.4	29.1	17.7	23.1	15.9	16.6	25.0
	3	27.9	30.4	11.1	36.9	9.2	24.4	16.8

LLV	Subject	Sensor locations						
		MV	Mid-S	AAr	XP	PV	AV	TV
V1 Time Location (ms)	1 W1	150	160	180	200	165	210	155
	1 W3					140	125	160
	1 W6	140	125	120	150	125	160	135
	2	170	130	135	195	130	175	130
	3	175	180	175	220	170	115	165
V2 Time Location (ms)	1 W1	575	470	505	520	500	495	475
	1 W3					485	525	475
	1 W6	555	565	585	540	480	595	565
	2	490	485	480	495	460	475	475
	3	455	415	545	485	430	480	435
V1 Time Width (ms)	1 W1	180	130	155	170	130	150	170
	1 W3					135	90	145
	1 W6	130	120	115	115	125	115	135
	2	175	95	95	180	100	80	140
	3	165	135	120	160	255	165	135
V2 Time Width (ms)	1 W1	155	100	145	150	160	195	120
	1 W3					130	150	235
	1 W6	135	160	125	285	135	145	155
	2	170	90	105	105	110	100	100
	3	235	165	240	175	115	145	155
V1 Center Frequency (Hz)	1 W1	10.1	13.0	17.0	12.0	15.7	15.0	12.0
	1 W3					17.4	28.0	10.8
	1 W6	12.8	16.4	22.0	14.3	21.1	8.5	12.8
	2	13.5	30.1	34.6	11.6	29.9	9.9	25.3
	3	14.5	6.0	6.9	8.6	5.9	7.1	10.2
V2 Center Frequency (Hz)	1 W1	6.2	4.5	12.8	9.5	14.6	15.4	9.7
	1 W3					4.5	17.4	9.3
	1 W6	10.1	7.5	6.0	6.0	26.4	5.8	8.5
	2	11.8	25.5	25.7	21.9	15.1	20.1	24.7
	3	8.3	5.1	6.1	6.4	6.6	5.5	11.6
V1 Frequency Width (Hz)	1 W1	13.1	17.2	20.9	9.5	24.8	18.4	16.8
	1 W3					16.6	23.1	8.5
	1 W6	15.4	27.8	12.4	15.5	20.0	11.2	16.9
	2	14.9	32.1	22.1	8.6	27.0	15.5	16.5
	3	15.2	14.8	11.9	22.5	15.9	11.7	14.4
V2 Frequency Width (Hz)	1 W1	21.0	7.9	15.5	17.4	20.1	28.8	13.7
	1 W3					11.3	10.5	11.9
	1 W6	19.8	19.9	10.6	13.6	15.6	12.2	22.3
	2	8.8	28.7	18.7	23.2	23.0	22.3	26.7
	3	22.7	5.7	21.5	9.2	12.3	12.5	23.5

VIII. REFERENCES

- [1] T. Vos *et al.*, "Global burden of 369 diseases and injuries in 204 countries and territories, 1990–2019: a systematic analysis for the Global Burden of Disease Study 2019," *The Lancet*, vol. 396, no. 10258, pp. 1204-1222, 2020.
- [2] S. Canada, "Leading causes of death, total population, by age group," ed: Statistics Canada Ottawa, ON, 2019.
- [3] S. Bae, S. R. Kim, M.-N. Kim, W. J. Shim, and S.-M. Park, "Impact of cardiovascular disease and risk factors on fatal outcomes in patients with COVID-19 according to age: a systematic review and meta-analysis," *Heart*, vol. 107, no. 5, pp. 373-380, 2021.
- [4] G. A. Roth *et al.*, "Global burden of cardiovascular diseases and risk factors, 1990–2019: update from the GBD 2019 study," *Journal of the American College of Cardiology*, vol. 76, no. 25, pp. 2982-3021, 2020.
- [5] F. Sana, E. M. Isselbacher, J. P. Singh, E. K. Heist, B. Pathik, and A. A. Armoundas, "Wearable devices for ambulatory cardiac monitoring: JACC state-of-the-art review," *Journal of the American College of Cardiology*, vol. 75, no. 13, pp. 1582-1592, 2020.
- [6] N. A. Trayanova, "Whole-heart modeling: applications to cardiac electrophysiology and electromechanics," *Circulation research*, vol. 108, no. 1, pp. 113-128, 2011.
- [7] S. Nattel, "New ideas about atrial fibrillation 50 years on," *Nature*, vol. 415, no. 6868, pp. 219-226, 2002.
- [8] C. Lee and L. Talbot, "A fluid-mechanical study of the closure of heart valves," *Journal of Fluid Mechanics*, vol. 91, no. 1, pp. 41-63, 1979.
- [9] M. Kundu, M. Nasipuri, and D. K. Basu, "Knowledge-based ECG interpretation: a critical review," *Pattern Recognition*, vol. 33, no. 3, pp. 351-373, 2000.
- [10] P. I. Aaronson, J. P. Ward, and M. J. Connolly, *The cardiovascular system at a glance*. John Wiley & Sons, 2020.
- [11] J. Reinhold and U. Rudhe, "Relation of the first and second heart sounds to events in the cardiac cycle," *British heart journal*, vol. 19, no. 4, p. 473, 1957.
- [12] A. Taebi, B. E. Solar, A. J. Bomar, R. H. Sandler, and H. A. Mansy, "Recent advances in seismocardiography," *Vibration*, vol. 2, no. 1, pp. 64-86, 2019.
- [13] I. Starr, A. Rawson, H. Schroeder, and N. Joseph, "Studies on the estimation of cardiac output in man, and of abnormalities in cardiac function, from the heart's recoil and the blood's impacts; the ballistocardiogram," *American Journal of Physiology-Legacy Content*, vol. 127, no. 1, pp. 1-28, 1939.
- [14] Y. D'Mello *et al.*, "Identification of the Vibrations Corresponding with Heart Sounds using Vibrational Cardiography," in *2020 42nd Annual International Conference of the IEEE Engineering in Medicine & Biology Society (EMBC)*, 2020: IEEE, pp. 17-20.
- [15] R. S. Crow, P. Hannan, D. Jacobs, L. Hedquist, and D. M. Salerno, "Relationship between seismocardiogram and echocardiogram for events in the cardiac cycle," *American journal of noninvasive cardiology*, vol. 8, pp. 39-46, 1994.
- [16] A. Taebi and H. A. Mansy, "Time-frequency distribution of seismocardiographic signals: A comparative study," *Bioengineering*, vol. 4, no. 2, p. 32, 2017.

-
- [17] M. AlGhatrif and J. Lindsay, "A brief review: history to understand fundamentals of electrocardiography," *Journal of community hospital internal medicine perspectives*, vol. 2, no. 1, p. 14383, 2012.
- [18] J. Achten and A. E. Jeukendrup, "Heart rate monitoring," *Sports medicine*, vol. 33, no. 7, pp. 517-538, 2003.
- [19] G. K. Prasad and J. Sahambi, "Classification of ECG arrhythmias using multi-resolution analysis and neural networks," in *TENCON 2003. Conference on convergent technologies for Asia-Pacific region*, 2003, vol. 1: IEEE, pp. 227-231.
- [20] T. Stamkopoulos, K. Diamantaras, N. Maglaveras, and M. Srintzis, "ECG analysis using nonlinear PCA neural networks for ischemia detection," *IEEE Transactions on Signal Processing*, vol. 46, no. 11, pp. 3058-3067, 1998.
- [21] S. Mansouri, T. Alhadidi, S. Chabchoub, and R. B. Salah, "Impedance cardiography: recent applications and developments," *Biomedical Research*, vol. 29, no. 19, pp. 3542-3552, 2018.
- [22] D. G. Newman and R. Callister, "The non-invasive assessment of stroke volume and cardiac output by impedance cardiography: a review," *Aviation, space, and environmental medicine*, vol. 70, no. 8, pp. 780-789, 1999.
- [23] M. Qu, Y. Zhang, J. G. Webster, and W. J. Tompkins, "Motion artifact from spot and band electrodes during impedance cardiography," *IEEE Transactions on Biomedical Engineering*, no. 11, pp. 1029-1036, 1986.
- [24] D. Tong, K. Bartels, and K. Honeyager, "Adaptive reduction of motion artifact in the electrocardiogram," in *Proceedings of the Second Joint 24th Annual Conference and the Annual Fall Meeting of the Biomedical Engineering Society*[[Engineering in Medicine and Biology, 2002, vol. 2: IEEE, pp. 1403-1404.
- [25] J. Allen, "Photoplethysmography and its application in clinical physiological measurement," *Physiological measurement*, vol. 28, no. 3, p. R1, 2007.
- [26] G. Lu, F. Yang, J. Taylor, and J. Stein, "A comparison of photoplethysmography and ECG recording to analyse heart rate variability in healthy subjects," *Journal of medical engineering & technology*, vol. 33, no. 8, pp. 634-641, 2009.
- [27] M. Nitzan, A. Romem, and R. Koppel, "Pulse oximetry: fundamentals and technology update," *Medical Devices (Auckland, NZ)*, vol. 7, p. 231, 2014.
- [28] Q. Yousef, M. Reaz, and M. A. M. Ali, "The analysis of PPG morphology: investigating the effects of aging on arterial compliance," *Measurement Science Review*, vol. 12, no. 6, p. 266, 2012.
- [29] B. S. Kim and S. K. Yoo, "Motion artifact reduction in photoplethysmography using independent component analysis," *IEEE transactions on biomedical engineering*, vol. 53, no. 3, pp. 566-568, 2006.
- [30] J. A. Patterson, D. C. McIlwraith, and G.-Z. Yang, "A flexible, low noise reflective PPG sensor platform for ear-worn heart rate monitoring," in *2009 sixth international workshop on wearable and implantable body sensor networks*, 2009: IEEE, pp. 286-291.
- [31] A. Leatham, "Phonocardiography," *British medical bulletin*, vol. 8, no. 4, pp. 333-342, 1952.
- [32] O. Al-Hamdani *et al.*, "Multimodal biometrics based on identification and verification system," *Journal of Biometrics & Biostatistics*, vol. 4, no. 2, pp. 1-8, 2013.

-
- [33] S. Ismail, I. Siddiqi, and U. Akram, "Localization and classification of heart beats in phonocardiography signals—a comprehensive review," *EURASIP Journal on Advances in Signal Processing*, vol. 2018, no. 1, pp. 1-27, 2018.
- [34] I. Sadek, J. Biswas, and B. Abdulrazak, "Ballistocardiogram signal processing: a review," *Health information science and systems*, vol. 7, no. 1, pp. 1-23, 2019.
- [35] O. T. Inan *et al.*, "Ballistocardiography and seismocardiography: A review of recent advances," *IEEE journal of biomedical and health informatics*, vol. 19, no. 4, pp. 1414-1427, 2014.
- [36] B. RM and K. LA, "Seismocardiography," *Kardiologiia*, vol. 4, pp. 87-89, 1964.
- [37] D. M. Salerno and J. Zanetti, "Seismocardiography for monitoring changes in left ventricular function during ischemia," *Chest*, vol. 100, no. 4, pp. 991-993, 1991.
- [38] D. M. Quarrie and P. Neary, "Comparison of seismocardiography to echocardiography for measuring cardiac cycle events," 2011.
- [39] M. Di Rienzo *et al.*, "Wearable seismocardiography: Towards a beat-by-beat assessment of cardiac mechanics in ambulant subjects," *Autonomic Neuroscience*, vol. 178, no. 1-2, pp. 50-59, 2013.
- [40] Y. D'Mello *et al.*, "Real-time cardiac beat detection and heart rate monitoring from combined seismocardiography and gyrocardiography," *Sensors*, vol. 19, no. 16, p. 3472, 2019.
- [41] M. Di Rienzo, E. Vaini, and P. Lombardi, "An algorithm for the beat-to-beat assessment of cardiac mechanics during sleep on Earth and in microgravity from the seismocardiogram," *Scientific reports*, vol. 7, no. 1, pp. 1-12, 2017.
- [42] M. Di Rienzo *et al.*, "Wearable seismocardiography for the beat-to-beat assessment of cardiac intervals during sleep," in *2014 36th Annual International Conference of the IEEE Engineering in Medicine and Biology Society*, 2014: IEEE, pp. 6089-6091.
- [43] I. Korzeniowska-Kubacka, B. Kuśmierczyk-Droszcz, M. Bilińska, B. Dobraszkievicz-Wasilewska, K. Mazurek, and R. Piotrowicz, "Seismocardiography—a non-invasive method of assessing systolic and diastolic left ventricular function in ischaemic heart disease," *Cardiology Journal*, vol. 13, no. 4, pp. 319-325, 2006.
- [44] K. Sørensen, S. E. Schmidt, A. S. Jensen, P. Søggaard, and J. J. Struijk, "Definition of fiducial points in the normal seismocardiogram," *Scientific reports*, vol. 8, no. 1, pp. 1-11, 2018.
- [45] K. Tavakolian, "Characterization and analysis of seismocardiogram for estimation of hemodynamic parameters," Applied Science: School of Engineering Science, 2010.
- [46] J. Skoric, *Respiratory Modulation of Sternal Accelerations*. McGill University (Canada), 2020.
- [47] Y. D'Mello *et al.*, "Autocorrelated differential algorithm for real-time seismocardiography analysis," *IEEE Sensors Journal*, vol. 19, no. 13, pp. 5127-5140, 2019.
- [48] A. Q. Javaid *et al.*, "Quantifying and reducing motion artifacts in wearable seismocardiogram measurements during walking to assess left ventricular health," *IEEE Transactions on Biomedical Engineering*, vol. 64, no. 6, pp. 1277-1286, 2016.
- [49] M. K. Azad, J. D'Angelo, P. T. Gamage, S. Ismail, R. H. Sandler, and H. A. Mansy, "Spatial Distribution of Seismocardiographic Signals," *Biomedical Signal Processing: Innovation and Applications*, p. 129.

-
- [50] K. Munck, K. Sørensen, J. J. Struijk, and S. E. Schmidt, "Multichannel seismocardiography: an imaging modality for investigating heart vibrations," *Physiological Measurement*, vol. 41, no. 11, p. 115001, 2020.
- [51] W.-Y. Lin *et al.*, "Identification of location specific feature points in a cardiac cycle using a novel seismocardiogram spectrum system," *IEEE journal of biomedical and health informatics*, vol. 22, no. 2, pp. 442-449, 2016.
- [52] I. InvenSense, "MPU-9250 Product Specification," ed: Revision, 2018.
- [53] E. Maiorana and C. Massaroni, "Biometric Recognition based on Heart-Induced Chest Vibrations," in *2021 IEEE International Workshop on Biometrics and Forensics (IWBF)*, 2021: IEEE, pp. 1-6.
- [54] P. K. Sahoo, H. K. Thakkar, and M.-Y. Lee, "A cardiac early warning system with multi channel SCG and ECG monitoring for mobile health," *Sensors*, vol. 17, no. 4, p. 711, 2017.
- [55] M. Di Rienzo, G. Rizzo, Z. M. İşilay, and P. Lombardi, "SeisMote: a multi-sensor wireless platform for cardiovascular monitoring in laboratory, daily life, and telemedicine," *Sensors*, vol. 20, no. 3, p. 680, 2020.
- [56] S. Majumder, T. Mondal, and M. J. Deen, "Wearable sensors for remote health monitoring," *Sensors*, vol. 17, no. 1, p. 130, 2017.
- [57] B. Karnath and W. Thornton, "Auscultation of the heart," *Hospital Physician*, vol. 38, no. 9, pp. 39-45, 2002.
- [58] M. Adcox. "Sternum Popping: Treatment, Pain, chest pain, and symptoms." <https://www.healthline.com/health/sternum-popping> (accessed August 8, 2021).
- [59] J. Skoric *et al.*, "Relationship of the Respiration Waveform to a Chest Worn Inertial Sensor," in *2020 42nd Annual International Conference of the IEEE Engineering in Medicine & Biology Society (EMBC)*, 2020: IEEE, pp. 2732-2735.
- [60] E. N. Marieb and K. Hoehn, *Human anatomy & physiology*. Pearson education, 2007.
- [61] K. Pandia, O. T. Inan, G. T. Kovacs, and L. Giovangrandi, "Extracting respiratory information from seismocardiogram signals acquired on the chest using a miniature accelerometer," *Physiological measurement*, vol. 33, no. 10, p. 1643, 2012.
- [62] B. S. Inc., "Application Note 109 1-, 3-, 6- and 12-Lead ECG ", 14 February 2019. Accessed: August 1, 2021. [Online]. Available: <https://www.biopac.com/application-note/ecg-ekg-electrocardiography-12-6-3-lead/>
- [63] A. Hulbert and P. Else, "Basal metabolic rate: history, composition, regulation, and usefulness," *Physiological and Biochemical Zoology*, vol. 77, no. 6, pp. 869-876, 2004.
- [64] J. Pan and W. J. Tompkins, "A real-time QRS detection algorithm," *IEEE transactions on biomedical engineering*, no. 3, pp. 230-236, 1985.
- [65] L. Luu and A. Dinh, "Artifact noise removal techniques on seismocardiogram using two tri-axial accelerometers," *Sensors*, vol. 18, no. 4, p. 1067, 2018.
- [66] J. Skoric, Y. D'Mello, M. Lortie, S. Gagnon, and D. V. Plant, "Effect of Static Respiratory Volume on the Waveform of Cardiac-induced Sternal Vibrations," in *2019 41st Annual International Conference of the IEEE Engineering in Medicine and Biology Society (EMBC)*, 2019: IEEE, pp. 4917-4921.
- [67] P. Dehkordi *et al.*, "Comparison of different methods for estimating cardiac timings: a comprehensive multimodal echocardiography investigation," *Frontiers in physiology*, vol. 10, p. 1057, 2019.

-
- [68] E. M. Johnson *et al.*, "Detecting aortic valve-induced abnormal flow with seismocardiography and cardiac MRI," *Annals of biomedical engineering*, vol. 48, no. 6, p. 1779, 2020.
- [69] B. Gramatikov, J. Brinker, S. Yi-Chun, and N. V. Thakor, "Wavelet analysis and time-frequency distributions of the body surface ECG before and after angioplasty," *Computer methods and programs in biomedicine*, vol. 62, no. 2, pp. 87-98, 2000.
- [70] S. Debbal, F. Berekci-Reguig, and A. M. Tani, "The fast Fourier transform and the continuous wavelet transform analysis of the phonocardiogram signal," *Journal of Mechanics in Medicine and Biology*, vol. 4, no. 03, pp. 257-272, 2004.
- [71] B. Ergen, Y. Tatar, and H. O. Gulcur, "Time-frequency analysis of phonocardiogram signals using wavelet transform: a comparative study," *Computer methods in biomechanics and biomedical engineering*, vol. 15, no. 4, pp. 371-381, 2012.
- [72] J. Kilby, G. Mawston, and H. G. Hosseini, "Continuous wavelet transform analysis for the classification of surface electromyography signals," in *World Congress on Medical Physics and Biomedical Engineering 2006, 2007*: Springer, pp. 1034-1036.
- [73] P. Kant, S. H. Laskar, J. Hazarika, and R. Mahamune, "CWT Based transfer learning for motor imagery classification for brain computer interfaces," *Journal of Neuroscience Methods*, vol. 345, p. 108886, 2020.
- [74] R. Büssow, "An algorithm for the continuous Morlet wavelet transform," *Mechanical Systems and Signal Processing*, vol. 21, no. 8, pp. 2970-2979, 2007.
- [75] L. M. Hari, G. Venugopal, and S. Ramakrishnan, "Analysis of Isometric Muscle Contractions using Analytic Bump Continuous Wavelet Transform," in *2020 42nd Annual International Conference of the IEEE Engineering in Medicine & Biology Society (EMBC)*, 2020: IEEE, pp. 732-735.
- [76] X. Zhang and R. Liu, "Analysis of Linear FM Signal Based on the STFT in the Filtering Viewpoint," in *2018 IEEE 3rd International Conference on Signal and Image Processing (ICSIP)*, 2018: IEEE, pp. 389-392.
- [77] Z. Peng, G. Meng, F. Chu, Z. Lang, W. Zhang, and Y. Yang, "Polynomial chirplet transform with application to instantaneous frequency estimation," *IEEE Transactions on Instrumentation and Measurement*, vol. 60, no. 9, pp. 3222-3229, 2011.
- [78] S. Mann and S. Haykin, "The chirplet transform: Physical considerations," *IEEE Transactions on Signal Processing*, vol. 43, no. 11, pp. 2745-2761, 1995.
- [79] G. Tu, "Chirplet Transform," MATLAB Central File Exchange, 2019. [Online]. Available: <https://www.mathworks.com/matlabcentral/fileexchange/72303-chirplet-transform>.
- [80] T. Royston, X. Zhang, H. Mansy, and R. Sandler, "Modeling sound transmission through the pulmonary system and chest with application to diagnosis of a collapsed lung," *The Journal of the Acoustical Society of America*, vol. 111, no. 4, pp. 1931-1946, 2002.
- [81] I. Vovk, V. Grinchenko, and V. Oleinik, "Modeling the acoustic properties of the chest and measuring breath sounds," *Acoustical physics*, vol. 41, no. 5, pp. 667-676, 1995.
- [82] S. B. Capps, R. C. Elkins, and D. M. Fronk, "Body surface area as a predictor of aortic and pulmonary valve diameter," *The Journal of thoracic and cardiovascular surgery*, vol. 119, no. 5, pp. 975-982, 2000.
- [83] K. Hergan, A. Schuster, M. Mair, R. Burger, and M. Töpker, "Normal cardiac diameters in cine-MRI of the heart," *RoFo: Fortschritte auf dem Gebiete der Rontgenstrahlen und der Nuklearmedizin*, vol. 176, no. 11, pp. 1599-1606, 2004.

-
- [84] A. I. Hassaballah, M. A. Hassan, A. N. Mardi, and M. Hamdi, "An inverse finite element method for determining the tissue compressibility of human left ventricular wall during the cardiac cycle," *Plos One*, vol. 8, no. 12, p. e82703, 2013.
- [85] C. E. Hampton and M. Kleinberger, "Material Models for the Human Torso Finite Element Model," US Army Research Laboratory Aberdeen Proving Ground United States, 2018.
- [86] Z. Li, M. W. Kindig, D. Subit, and R. W. Kent, "Influence of mesh density, cortical thickness and material properties on human rib fracture prediction," *Medical engineering & physics*, vol. 32, no. 9, pp. 998-1008, 2010.
- [87] F. Fidanza, "Body fat in adult man: semicentenary of fat density and skinfolds," *Acta diabetologica*, vol. 40, no. 1, pp. s242-s245, 2003.
- [88] Y. Lee and K. Hwang, "Skin thickness of Korean adults," *Surgical and radiologic anatomy*, vol. 24, no. 3-4, pp. 183-189, 2002.
- [89] H. Kanai, "Propagation of vibration caused by electrical excitation in the normal human heart," *Ultrasound in medicine & biology*, vol. 35, no. 6, pp. 936-948, 2009.
- [90] A. Grunovas, E. Trinkunas, A. Buliuolis, E. Venskaityte, J. Poderys, and K. Poderiene, "Cardiovascular response to breath-holding explained by changes of the indices and their dynamic interactions," *Biol. Syst. Open Access*, vol. 5, p. 152, 2016.
- [91] M. J. Joyner, "Effect of exercise on arterial compliance," ed: Am Heart Assoc, 2000.
- [92] C. J. Lavie, C. Ozemek, S. Carbone, P. T. Katzmarzyk, and S. N. Blair, "Sedentary behavior, exercise, and cardiovascular health," *Circulation research*, vol. 124, no. 5, pp. 799-815, 2019.
- [93] R. Fagard, "Athlete's heart," *Heart*, vol. 89, no. 12, pp. 1455-1461, 2003.
- [94] D. L. Sikarskie, P. D. Stein, and M. Vable, "Mathematical model of aortic valve vibration," in *Mathematical Modelling in Science and Technology*: Elsevier, 1984, pp. 709-714.
- [95] K. O. Lim, Y.-C. Liew, and C.-H. Oh, "Analysis of mitral and aortic valve vibrations and their role in the production of the first and second heart sounds," *Physics in Medicine & Biology*, vol. 25, no. 4, p. 727, 1980.
- [96] O. J. Kemi, J. P. Loennechen, U. Wisløff, and Ø. Ellingsen, "Intensity-controlled treadmill running in mice: cardiac and skeletal muscle hypertrophy," *Journal of applied physiology*, vol. 93, no. 4, pp. 1301-1309, 2002.
- [97] G. A. Holzapfel, T. C. Gasser, and R. W. Ogden, "A new constitutive framework for arterial wall mechanics and a comparative study of material models," *Journal of elasticity and the physical science of solids*, vol. 61, no. 1, pp. 1-48, 2000.
- [98] M. Amabili *et al.*, "Nonlinear dynamics of human aortas for material characterization," *Physical Review X*, vol. 10, no. 1, p. 011015, 2020.
- [99] Z. Dai, Y. Peng, H. A. Mansy, R. H. Sandler, and T. J. Royston, "Comparison of poroviscoelastic models for sound and vibration in the lungs," *Journal of vibration and acoustics*, vol. 136, no. 5, 2014.